DEPARTMENT OF MECHANICAL ENGINEERING AND MECHANICS
COLLEGE OF ENGINEERING AND TECHNOLOGY
OLD DOMINION UNIVERSITY
NORFOLK, VIRGINIA 23508

SUPERSONIC AERODYNAMIC INTERFERENCE EFFECTS OF STORE SEPARATION, PART I: COMPUTATIONAL ANALYSIS OF CAVITY FLOWFIELDS

By

Oktay Baysal, Principal Investigator

Final Report
For the period May 16, 1985 to July 15, 1986

Prepared for the
National Aeronautics and Space Administration
Langley Research Center
Hampton, VA 23665

Under
NASA Research Grant NAG-1-559
Wallace C. Sawyer, Technical Monitor
HSAD-Fundamental Aerodynamics Branch

September 1986

DEPARTMENT OF MECHANICAL ENGINEERING AND MECHANICS
COLLEGE OF ENGINEERING AND TECHNOLOGY
OLD DOMINION UNIVERSITY
NORFOLK, VIRGINIA 23508

SUPERSONIC AERODYNAMIC INTERFERENCE EFFECTS OF STORE SEPARATION, PART I: COMPUTATIONAL ANALYSIS OF CAVITY FLOWFIELDS

By

Oktay Baysal, Principal Investigator

Final Report
For the period May 16, 1985 to July 15, 1986

Prepared for the
National Aeronautics and Space Administration
Langley Research Center
Hampton, VA 23665

Under
NASA Research Grant NAG-1-559
Wallace C. Sawyer, Technical Monitor
HSAD-Fundamental Aerodynamics Branch

Submitted by the
Old Dominion University Research Foundation
P. O. Box 6369
Norfolk, Virginia 23508

September 1986

TABLE OF CONTENTS

LIST OF FIGURES

TABLE OF CONTENTS - continued

LIST OF FIGURES - continued

TABLE OF CONTENTS - continued

LIST OF FIGURES - continued

TABLE OF CONTENTS - continued

LIST OF FIGURES - continued

LIST OF SYMBOLS

a	local speed of sound
d, D	cavity depth
E	energy per unit volume
EMAC	explicit-implicit MacCormack
f	external force per unit volume
h	cavity height (used interchangeably with cavity depth, d)
I	unit diagonal matrix
J	transformation Jacobian
k	turbulent energy
K	heat conductivity
L	cavity length
M	Mach number
m	momentum
p	pressure
Pr	Prandtl number
R	specific gas constant
Re	Reynolds number
t	time
T	temperature
ULGSR	upwind line Gauss-Seidel relaxation
u	x-direction velocity component
V	velocity vector
v	y-direction velocity component
w	cavity width
x,y	cartesian coordinates

Greek symbols

γ	ratio of specific heats

ε	turbulent dissipation
λ	second coefficient of viscosity (bulk)
μ	first coefficient of viscosity (molecular)
ρ	density
τ	viscous stress term
ω	vorticity

Subscripts

m	molecular value
o	stagnation
t	turbulent
v	viscous sublayer
w	wall
∞	freestream

Constants

C_ℓ, C_p, C_T, C_μ, $C_{\varepsilon 1}$, $C_{\varepsilon 2}$, S_a, S_b, β, κ, σ_k, σ_ε

SUPERSONIC AERODYNAMIC INTERFERENCE EFFECTS OF STORE SEPARATION, PART I: COMPUTATIONAL ANALYSIS OF CAVITY FLOWFIELDS

By

Oktay Baysal*

1. INTRODUCTION AND BRIEF REVIEW OF EXISTING WORK

The first phase of the investigation is devoted to the study of the cavity flowfields. It is aimed at developing a predictive method based on a rational model of the cavity flowfield to obtain sufficiently accurate velocity and pressure field determination needed to predict store motion while in the region of influence of the cavity.

The simulation efforts are being conducted in two steps. The first step is the simulation of a two-dimensional cavity, that is, the width is considered infinitely long. Such an exercise is intended to be educational in understanding the flow behavior around the leading edge, the front face, the ceiling, and the rear face of the cavity, the formation of the shear layer, its deflection and bridging characteristic, the possible interactions of the shear layer, the boundary layer and shock waves. Due to the symmetry of the flowfield with respect to the h-L-plane at w/2, two-dimensional simulations represent the flow at this particular plane where the third dimension effects are eliminated (Fig. 1). When sufficient learning experience is achieved, and necessary confidence in the preliminary two-dimensional code is acquired, the final step of the cavity flowfield study, that is, the three-dimensional cavity, will be initiated.

Supersonic cavity flowfields, in the broadest sense, have been

*Assistant Professor, Department of Mechanical Engineering and Mechanics, Old Dominion University, Norfolk, Virginia 23508.

investigated experimentally by Stallings et al. (Refs. 1 and 2) at NASA Langley Research Center. There exist empirical formulae suggested by earlier reports (Refs. 3, 4, and 5). More recent experimental studies have been conducted by both U.S. Air Force and Soviet researchers (Refs. 7-9). Sources of interest of these studies varied from store separation to acoustics and heat transfer.

Flow Mach numbers used vary from 0.3 to 6.0. Among the measured quantities were shock wave pulsations and heat transfer coefficient. Varfolomeyev et al. (Ref. 9) observed the vortices mentioned above in their experiments. McGregor et al. (Ref. 6) proposed a drag coefficient relation for the cavity and concluded that the effect of the wind tunnel was on the strength of the pressure waves but not on their patterns. Wind tunnel effects diminished with increases in flow Mach number. Sinha et al.(Ref. 7) concluded that the free shear region showed self-similarity and the recirculating flow had the character of a wall jet in the reverse direction superimposed on a forward moving free shear layer. With the more efficient application of numerics and advanced computational resources, analytical simulations of the cavity flowfields started appearing in the literature (Refs. 10-16). Although these efforts are presently restricted by assumptions, such as, inviscid, laminar, incompressible, two-dimensional, or only certain length-to-height ratios, more complete studies are in the development stage at present.

2. DESCRIPTION OF PHYSICAL AND MATHEMATICAL MODELS

Flow Development:

With the separation of the store, a cavity is created in the oncoming

supersonic flow. This causes a significant increase in the fluid-dynamic, fluid-resonant drag, and generate fluid-elastic oscillations. The forward corners generate the velocity and pressure fluctuations which are amplified during the expansion and the convection of the flow downstream. The oncoming viscous flow will separate from the cavity forward edge, generating the highly vortical shear layer around the top and counter rotating eddies near the bottom corners as a result of the adjustment of the shear and pressure forces acting on the recirculating fluid to the no-slip condition imposed by the walls. Viscous forces acting near body surfaces can reduce the momentum of the fluid in a thin boundary layer region, so that when acted upon by inertial forces, the boundary layer separates from the body. Depending on the length-to-depth ratio the flow field inside the cavity varies (Fig. 2). In deeper geometries, the cavity may be bridged by the shear layer which is inherently unstable (open cavity.) In shallower geometries, the shear layer is deflected inwards with a possible reattachment point at the bottom of the cavity (closed cavity). The resonant effects are associated with compressibility or free surface wave phenomena. The solid boundary may engage in an elastic motion coupling with the flow oscillations.

Longitudinal vortices (Taylor-Görtler like vortices) originate in the zone of separation between the primary eddy and the downstream secondary eddy, and are convected around the cavity. This separated shear layer is continuously pulled into and pushed out of the cavity. When the cavity resonates the shear layer is deflected and pumps mass (carrying significant momentum) into the cavity. This ingested mass is slowed down by various dissipative processes within the cavity. Its presence causes the cavity pressure to exceed the freestream pressure. The shear layer is then deflected out of the cavity by the excess pressure and mass is pumped out of

the cavity with low momentum. This oscillatory process extracts additional freestream momentum during the cycle. The combination of pressure drag (due to the cavity walls) and momentum drag (due to the transient eddy cycle) can represent a violent oscillating force on the body. Furthermore, this flowfield becomes dominated by regions of separated flow within a mixed locally subsonic and supersonic flow.

The shallow cavity flow poses an added complexity to the overall flow picture when the shear layer is deflected enough to touch the ceiling of the cavity (Fig. 3). The inward bound flow is turned by a series of Mach waves which in turn coalesce into a shock. An adverse pressure gradient is generated by such compression waves, which causes a secondary separation from the ceiling of the cavity. Due to the oscillatory behavior of the flowfield the points of separation and reattachment are periodic in time.

Mathematical Statement

As it is evident from the results of the experimental studies mentioned above, the flow field includes expansions, shocks, separations, recirculations, and reattachments. The computational simulation of this fluid-dynamically rather complex flow field requires the inclusion of viscous terms, modelling of turbulence, regionally clustered gridding, and a shock treatment mechanism. Fully conservative Navier-Stokes equations are written in generalized-curvilinear coordinates to enhance the flow adaptiveness. The structure of the turbulence is modelled by the modified k-ε model (ref. 3) for recirculating flows. Shocks are captured using the divergence of velocity test and treated by the artificial dissipative terms.

The boundary conditions imposed at the solid walls are the conventional

impermeability and no-slip conditions. The wall temperature is assumed to be the stagnation temperature (adiabatic wall). The pressure gradient normal to the surface is assumed to be zero, however, the gradient parallel to the surface is computed from the momentum equation. Downstream and outer boundaries are computed from the computation zone values by first-degree extrapolation (extrapolation of property gradients). The upstream boundary is either assumed to have property profiles computed by a boundary layer code, or assumed to be at free stream conditions, thence, a leading edge shock. To initialize the computation, the variables all over the computation zone are given the values of the upstream boundary (to save computation time), with the exception of the points inside the cavity, where the flow is assumed stagnant initially.

General form of the fluid flow equations:

$$\frac{\partial \rho}{\partial t} + \nabla \cdot \vec{M} = 0 \tag{1}$$

$$\frac{\partial \vec{M}}{\partial t} + \nabla \cdot \left(\frac{\vec{M}\vec{M}}{\rho} - \bar{\bar{\sigma}} \right) = \vec{f} \tag{2}$$

$$\frac{\partial E}{\partial t} + \nabla \cdot \left(E \vec{V} - \bar{\bar{\sigma}} \vec{V} + \vec{q} \right) = \vec{f} \cdot \vec{V} \tag{3}$$

Perfect Gas Law:

$$p = \rho RT = (\gamma - 1) \left(E - \frac{1}{2} \rho \vec{V}^2 \right) \tag{4}$$

where

$$\vec{M} = \rho \vec{V} \quad , \quad \vec{q} = - k (\nabla T), \tag{5}$$

Newtonian Fluid Stress-Strain Relations:

$$\bar{\bar{\sigma}} = - \rho \bar{\bar{I}} + \bar{\bar{\tau}} \quad , \quad \bar{\bar{\tau}} = \lambda \nabla \cdot \vec{V} \bar{\bar{I}} + \mu [\nabla \vec{V} + (\nabla \vec{V})^T] \tag{6}$$

The governing fluid motion equations are derived featuring the following:

- strong conservation form
- transformed into generalized curvilinear coordinate system (ξ,η)
- k-ϵ turbulence modeling or two-layer algebraic turbulence model
- two-dimensional
- artificial dissipative terms proportional to the second gradient of pressure and temperature, and controlled with blending constants
- molecular viscosity from Sutherland law

$$\frac{\partial U_1}{\partial t} + \frac{\partial F_1}{\partial \xi} + \frac{\partial G_1}{\partial \eta} = H \tag{7}$$

where

$$U_1 = U/J, \quad F_1 = [(F + S_1) \xi_x + (G + S_2) \xi_y]/J \tag{8}$$

$$G_1 = [F + S_1) \eta_x + (G + S_2) \eta_y]/J \tag{9}$$

and

$$U = \begin{bmatrix} \rho \\ \rho u \\ \rho v \\ E \\ \rho k \\ \rho \varepsilon \end{bmatrix}, \qquad F = \begin{bmatrix} \rho u \\ \rho u^2 + \rho - \tau_{xx} \\ \rho uv \\ u(E + \rho - \tau_{xx}) - v\,\tau_{xy} - q_x \\ \rho uk - D_{xk} \\ \rho u\varepsilon - D_{ex} \end{bmatrix}$$

$$G = \begin{bmatrix} \rho v \\ \rho uv - \tau_{xy} \\ \rho v^2 + p - \tau_{yy} \\ v\,(E + \lambda - \tau_{yy}) - u\tau_{xy} - q_y \\ \rho vk - D_{ky} \\ \rho v\varepsilon - D_{\varepsilon y} \end{bmatrix}, \qquad H = \begin{bmatrix} 0 \\ 0 \\ 0 \\ 0 \\ \rho(P - \varepsilon) \\ \rho \frac{\varepsilon}{k}(C_{\varepsilon 1} P - C_{\varepsilon 2}\varepsilon) \end{bmatrix}$$

$$\tau_{xx} = (2\mu + \lambda)\frac{\partial u}{\partial x} + \lambda \frac{\partial v}{\partial y} - \frac{2}{3}\rho k \tag{10}$$

$$\tau_{xy} = \mu\left(\frac{\partial u}{\partial y} + \frac{\partial v}{\partial x}\right) \tag{11}$$

$$\tau_{yy} = (2\mu + \lambda)\frac{\partial v}{\partial y} + \lambda \frac{\partial u}{\partial x} - \frac{2}{3}\rho k \tag{12}$$

$$q_x = K\frac{\partial T}{\partial x}, \qquad q_y = K\frac{\partial T}{\partial y} \tag{13}$$

$$D_{kx} = \left(\frac{\mu_t}{\sigma_k} + \mu_m\right)\frac{\partial k}{\partial x}, \qquad D_{ky} = \left(\frac{\mu_t}{\sigma_k} + \mu_m\right)\frac{\partial k}{\partial y} \tag{14}$$

$$D_{\varepsilon x} = \left(\frac{\mu_t}{\sigma_\varepsilon} + \mu_m\right) \frac{\partial \varepsilon}{\varepsilon x} \quad , \quad D_{\varepsilon y} = \left(\frac{\mu_t}{\sigma_\varepsilon} + \mu_m\right) \frac{\partial \varepsilon}{\partial y} \tag{15}$$

$$p = \frac{\mu_t}{\rho}\left[2\left(\frac{\partial u}{\partial x}\right)^2 + \left(\frac{\partial v}{\partial y}\right)^2 + \left(\frac{\partial u}{\partial y} + \frac{\partial v}{\partial x}\right)^2 - \frac{2}{3}\left(\frac{\partial u}{\partial x} + \frac{\partial v}{\partial y}\right)^2\right] - \frac{2}{3} k \left(\frac{\partial u}{\partial x} + \frac{\partial v}{\partial y}\right) \tag{16}$$

$$\mu_t = \rho\, c_\mu\, k^2/\varepsilon \quad , \quad K_t = \frac{\gamma R}{\gamma - 1} \frac{\mu_t}{Pr_t} \tag{17}$$

$$\mu_m = \frac{s_a T^{3/2}}{s_b + T} \quad , \quad K_m = \frac{\gamma R}{\gamma - 1} \frac{\mu_m}{Pr_m} \tag{18}$$

$$\mu = \mu_m + \mu_t \quad , \quad K = K_m + K_t \tag{19}$$

$$S_1 = (\Delta x)^4 \left(\frac{\partial U}{\partial x}\right)(|u| + a)\left[\frac{C_p}{4p}\frac{\partial^2 p}{\partial x^2} + \frac{C_T}{4T}\frac{\partial^2 T}{\partial x^2}\right] \tag{20}$$

$$S_2 = (\Delta y)^4 \left(\frac{\partial U}{\partial y}\right)(|v| + a)\left[\frac{C_p}{4p}\frac{\partial^2 P}{\partial y^2} + \frac{C_T}{4T}\frac{\partial^2 T}{\partial y^2}\right] \tag{21}$$

The Jacobian and the metrics are written as follows and obtained numerically from the grid generated for each node:

$$J = \frac{\partial(\xi, \eta)}{\partial(x, y)} = \xi_x \eta_y - \xi_y \eta_x = (x_\xi y_\eta - y_\xi x_\eta)^{-1} \qquad (22)$$

and

$$\xi_x = J(y_\eta) \quad , \quad \xi_y = - J(x_\eta) \qquad (23)$$

$$\eta_x = - J(y_\xi) \quad , \quad \eta_y = J(x_\xi) \qquad (24)$$

Turbulence Models:

Since the $k - \varepsilon$ turbulence model is devised for high Reynolds number number flows, a wall function (Ref. 19) is adopted and used for the very low Reynolds numbers regions near the walls (Fig. 4). The procedure of using this wall function may be summed up as follows:

1. velocity profile from previous time step, $u=f(y)$, $v=f(y)$

2. $$k(y) = \left(\frac{\kappa}{\sqrt{C_\mu}}\, y\right)^2 \frac{\partial u}{\partial y}$$

3. $$y_v = \frac{(Re_v)\nu}{\sqrt{k_v}} \quad , \quad Re_v \cong 20$$

4. $$\tau_w = \kappa \rho u_{w+1} \sqrt{k_v} \,/\, [\ln E^* Re_v] \quad , \quad E^* = e^{\kappa/Re_v} / Re_v$$

$$\tau_{w+2} = \mu \left(\frac{\partial u}{\partial y} + \frac{\partial v}{\partial x}\right)_{w+2}$$

5. Assume linear variation of τ, i.e.

$$\tau_{w+1} = \tau_w + \frac{\tau_{w+2} - \tau_w}{y_{w+2} - y_w} (y_{w+1} - y_w)$$

6. $$\mu_{w+1} = \frac{\tau_{w+1}}{\left(\frac{\partial u}{\partial y} + \frac{\partial v}{\partial x}\right)_{w+1}} = (\mu_m + \mu_t)_{w+1}$$

7. $$\varepsilon_{w+1} = k_{w+1}^{3/2} / C_\ell (y_{w+1} - y_w)$$

8. $$k_{w+1} = (\rho C_\mu \varepsilon_{w+1})^{1/2}$$

Assume within the viscous sublayer:

$$\begin{matrix} u' = a(t)\, y \\ v' = b(t)\, y \end{matrix} \rightarrow k = \overline{\left(\frac{a^2 + b^2}{2}\right)} y^2, \qquad \text{near the wall}$$

The derived equations above are subject to the following initial and boundary conditions:

initial conditions:

- a given boundary layer profile, $\vec{V} = \vec{V}(y)$

with $\vec{V}(y \geq \sigma) = U_\infty \vec{i}$

- $p = p_\infty, \quad \rho = \rho_\infty$

- Compute E and T profiles from $\vec{V}(y)$

$$T = T_\infty - \frac{\vec{V}^2}{(2\gamma R/\gamma - 1)}$$

$$E = \rho \left[\frac{R}{\gamma - 1} T + \frac{1}{2} \vec{V}^2\right]$$

- k, ε:

$$U_\infty \frac{Dk_\infty}{dx} = - \varepsilon_\infty$$

$$U_\infty \frac{d\varepsilon_\infty}{dx} + 2 f_2 \varepsilon_\infty^2 / k_\infty$$

where

$$f_2 = 1 - 0.3 \exp[-\rho k^2/\mu\varepsilon)^2]$$

upstream boundary:

same as initial conditions

solid wall:

$\vec{V}_w = 0$ no-slip, impermeable

$\left(\frac{\partial q}{\partial n}\right)_{wall} \cong 0$ adiabatic wall, where n is the normal direction to the wall

$$\frac{\partial p}{\partial x} = \frac{\partial \tau_{xx}}{\partial x} + \frac{\partial \tau_{xy}}{\partial y} \quad \rightarrow \quad p_w$$

Compute ρ_w

$$\varepsilon_w = k_w = 0$$

downstream and outer boundary:

- first degree extrapolation from the computation zone, i.e. gradient of a primitive variable at the boundary is equal to the gradient of that variable at the neighboring internal point.

In view of the upcoming three dimensional simulations, where computer storage and CPU time may become limiting constraints, a two-layer algebraic turbulence model of Baldwin and Lomax (Ref. 20) is also built in as an option. When this option is turned on the k-ε equations are 'blanked out'.

Turbulence of the wall shear flow is called the inner turbulence, and it is modeled using the Prandtl mixing length theory with the improvement of the Van Driest formulation. Using the nomenclature of Baldwin and Lomax, inner eddy viscosity coefficient is calculated as

$$(\mu_t)_{inner} = \rho \ell^2 |\omega| \tag{25}$$

where

$$\ell \equiv 0.4y \left[1 - \exp\left(-y^+/26\right)\right] \tag{26}$$

and $$y^+ = (\rho_w \ \tau_w)^{\frac{1}{2}} \ y/\mu_w \tag{27}$$

where y is the local normal distance from a solid surface.

Turbulence of the outer region is based on the Clauser formulation using the Klebanoff approximation to the Gaussian error function that gives the intermittency factor. The outer eddy viscosity coeficient is calculated as

$$(\mu_t)_{outer} = 0.0269 \ \rho \ F_{wake} \ F_{kleb} \tag{28}$$

where the value of F_{kleb}, the Klebanoff intermittency factor, is given by

$$F_{kleb} = [1 + 5.5 \ (0.3 \ y/Y_{max})^6]^{-1} \tag{29}$$

and

$$F(y) = y \ |\omega| \ [1 - \exp \ (- \ y^+/26)] \tag{30}$$

where $F(y)$ is maximum, F_{max}, at $y = Y_{max}$. F_{wake} is the minimum of $(Y_{max} \ F_{max})$ or $(0.25 \ Y_{max} \ U^2_{dif}/F_{max})$, where

$$U_{dif} = \{\max \ [\vec{M}/\rho] - \min \ [\vec{M}/\rho]\} \tag{31}$$

at a fixed tangential location. The crossover point, where the switch is made from $(\mu_t)_{outer}$ to $(\mu_t)_{inner}$, is the minimum value of y where $(\mu_t)_{outer}$ to $(\mu_t)_{inner}$, is the minimum value of y where $(\mu_t)_{outer}$ becomes less than $(\mu_t)_{inner}$.

3. COMPUTATIONAL METHODS

Explicit-Implicit MacCormack Scheme: (EMAC):

Since the mainstream flow is supersonic, the set of partial differential equations (7) are predominantly hyperbolic. Therefore, the explicit-implicit scheme of MacCormack (Ref. 21), which is developed for hyperbolic equations, is one of the methods adopted. The method is second-order accurate both in time and space which is achieved through using predictor and corrector steps. Each step is consisted of an explicit substep and an implicit step. The reasons for this substepping are: (1) reduce tridiagonal flux Jacobian matrices to bidiagonal matrices and apply direct solution, (2) when time step Δt meets the stability criterion (CFL), the implicit substeps which require most of the computation time are automatically bypassed, thence an explicit scheme.

$|\hat{A}|$ and $|\hat{B}|$ are matrices with positive eigenvalues, related to the Jacobians

$$\hat{A} = (\partial\hat{F}/\partial\hat{U}) \quad \text{and} \quad \hat{B} = \partial G/\partial\hat{U}).$$

$(\Delta^+/\Delta\xi)$ and $(\Delta^+/\Delta\eta)$ are one-sided forward differences.

$(\Delta^-/\Delta\xi)$ and $(\Delta^-/\Delta\eta)$ are one-sided backward differences.

The Jacobians A and B are related to the Jacobian $A = \partial F/\partial U$ and $B = \partial G/\partial U$ by

$$\begin{aligned} \hat{A} &= A\xi_x + B\xi_y \\ \hat{B} &= A\eta_x + B\eta_y \end{aligned} \tag{32}$$

1. Explicit Predictor Step:

$$\Delta \hat{U}_{ij}^{n} = -\Delta t \left[\frac{\Delta^{+} F_{ij}^{n}}{\Delta \xi} + \frac{\Delta^{+} G_{ij}^{n}}{\Delta \eta} \right] \quad \text{at every point inside the calculation domain} \tag{33}$$

where $\Delta \hat{U}_{ij}^{n} = \{ U_{ij}^{n+1} - U_{ij}^{n} \}$

2. Implicit Predictor Step:

$$\text{Solve} \left[I - \Delta t \frac{\Delta^{+} |\hat{A}|^{n}}{\Delta \xi} \right] \left[I - \Delta t \frac{\Delta^{+} |\hat{B}|}{\Delta \eta} \right] \delta \hat{U}_{ij}^{\overline{n+1}} = \Delta \hat{U}_{ij}^{n} \tag{34}$$

for $\delta \hat{U}_{ij}^{\overline{n+1}}$.

This is done in two steps.

Let

$$\delta \hat{U}_{ij}^{*} = I - \Delta t \, \Delta^{+} \frac{|\hat{B}|}{\Delta \eta} \, \delta \hat{U}_{ij}^{\overline{n+1}} . \tag{35}$$

This results in two equations, namely,

$$\text{a)} \quad \left[I - \Delta t \frac{\Delta^{+} |\hat{A}|^{n}}{\Delta \xi} \right] \delta \hat{U}_{ij}^{*} = \Delta \hat{U}_{ij}^{n} \tag{36}$$

b) $$\left[I - \Delta t \ \frac{\Delta^+ \ |\hat{B}|^n}{\Delta \eta} \right] \delta \hat{U}_{ij}^{n+1} = \delta \xi_{ij}^{*} \tag{37}$$

The above two equations can be solved by splitting $|\hat{A}|$ to $S_\xi \ D_A \ S_\xi^{-1}$ as,

$$I - \Delta t \left[\frac{\Delta^+ \ |\hat{A}|^n}{\Delta \xi} \right] \delta \hat{U}_{ij}^{*} = \Delta \hat{U}_{ij}^{n}. \tag{38}$$

Now this equation may be simplified by algebraic manipulation as,

$$I - \Delta t \left[|\hat{A}|_{i+1,j}^{n} - |\hat{A}|_{i,j}^{n} \right] \delta \hat{U}_{ij}^{*} = \Delta \hat{U}_{ij}^{n} \tag{39}$$

$$I + \{\Delta t \ |\hat{A}|_{ij}^{n}\} \ \delta u_{ij}^{*} = \Delta U_{ij}^{n} + \Delta t \ |\hat{A}|_{i+1,j}^{n} \ (\delta U_{ij}^{*}). \tag{40}$$

But $|\hat{A}|^n = S_\xi \ D_A \ S_\xi^{-1}$

$$\{I + \Delta t \ S_{\xi ij} \ D_{Aij} \ S_{\xi ij}^{-1}\} \ \delta \hat{U}_{ij}^{*}$$

$$= \Delta \hat{U}_{ij}^{n} + \Delta t \ |\hat{A}|_{i+1,j} \ \delta \hat{U}_{i+1,j}^{*} \ . \tag{41}$$

Let $W = \Delta \hat{U}_{ij}^{n} + \Delta t \ |\hat{A}|_{i+1,j} \ \delta \hat{U}_{i+1,j}^{*}$, then

$$\delta \hat{U}_{ij}^{*} = \hat{S}_\xi \ (I + \Delta t D_A)^{-1} \ \hat{S}_\xi^{-1} \ W \tag{42}$$

This equation can be easily solved since S_ξ and S_ξ^{-1} are known and the inversion of the diagonal matrix $(I+\Delta t D_A)$ is routine. After all δU^*_{ij} inside the computation domain are determined the step (b) is carried out in the same manner. Corrector steps are analogous to predictor steps.

The details of methodology are included in Appendix.

Line Gauss-Seidel Upwind Relaxation Scheme (ULGSR):

In the MacCormack scheme explained above, dissipative terms are added for numerical stablity. Often the optimal determination of these terms is not straightforward. Furthermore, such terms cause the "smearing" of the solution at large-gradient zones and may cause drainage of the conserved properties.

Recently, there has been considerable progress in the development of upwind methods, which recognize the hyperbolic nature of the time-dependent inviscid equations in the construction of naturally dissipative schemes. The improvement in physical treatment comes generally at the expense of increased computational work in comparison to central difference approximations. However, improved algorithms tailored to the properties of the upwind discretization are being developed. The diagonally dominant properties of coefficient matrices arising from such discretizations allow efficient relaxation procedures to be developed which can increase the overall convergence rate, and thus offset the increased computational work per time step (Refs. 22 and 23).

An efficient relaxation algorithm for the Navier-Stokes equations is obtained by using upwind differencing for the convective and pressure terms and central differencing for the viscous shear and heat flux terms. The

upwind differencing in the present work is implemented using the flux splitting method developed by Van Leer including third-order accurate spacial differencing, although the techniques described could be applied to most upwind difference methods.

Rewriting Eq. 7 with slightly different nomenclature is convenient at this point.

$$\frac{\partial \hat{Q}}{\partial t} + \frac{\partial \hat{G}}{\partial \eta} + \frac{\partial \hat{H}}{\partial \zeta} + \overline{Re}^{-1}\{\partial_\eta[J^{-1}(\eta_x R + \eta_y S)] + \partial_\zeta[J^{-1}(\zeta_x R + \zeta_y S)]\} \tag{43}$$

$$\begin{aligned} \hat{Q} &= Q/J \\ \hat{G} &= (\eta_x G + \zeta_y H)/J \\ \hat{H} &= (\zeta_x G + \zeta_y H)/J \end{aligned} \tag{44}$$

$$Q = \begin{bmatrix} \rho \\ \rho u \\ \rho v \\ E \end{bmatrix} \qquad G = \begin{bmatrix} \rho u \\ \rho u^2+p \\ \rho uv \\ u(E+p) \end{bmatrix} \qquad H = \begin{bmatrix} \rho v \\ \rho uv \\ \rho v^2+p \\ v(E+p) \end{bmatrix} \tag{45}$$

where η is the coordinate along the body and ζ is the coordinate normal to the body.

The viscous terms on the right-hand side are given by

$$R = \begin{bmatrix} 0 \\ \tau_{xx} \\ \tau_{xy} \\ R_4 \end{bmatrix} \qquad S = \begin{bmatrix} 0 \\ \tau_{xy} \\ \tau_{yy} \\ S_4 \end{bmatrix} \tag{46}$$

$$\tau_{xx} = (\lambda+2\mu)\ (\eta_x\ u_\eta + \zeta_x u_\zeta) + \lambda(\eta_y v_\eta + \zeta_y v_\zeta) \tag{47}$$

$$\tau_{yy} = (\lambda+2\mu)\ (\eta_y\ v_\eta + \zeta_y\ v_\zeta) + \lambda(\eta_x u_\eta + \zeta_x u_\zeta) \tag{47a}$$

$$\tau_{xy} = \mu(\eta_y u_\eta + \zeta_y u_\zeta + \eta_x v_\eta + \zeta_x\ v_\zeta) \tag{47b}$$

$$R_4 = u\tau_{xx} + v\tau_{xy} + \mu Pr^{-1}(\gamma-1)^{-1}\ (\eta_x \partial_\eta a^2 + \zeta_x \partial_\zeta a^2) \tag{47c}$$

$$S_4 = u\tau_{xy} + v\tau_{yy} + \mu Pr^{-1}(\gamma-1)^{-1}(\eta_y\ \partial_\eta\ a^2 + \zeta_y\ \partial_\xi a^2) \tag{47d}$$

An implicit, upwind, finite-volume scheme described in Refs. 22 and 23 is used to solve (1). Application of approximate factorization allows the system of equations to be solved in two sweeps:

$$[\frac{I}{J\Delta t} + \partial_\eta{}^{-}A^{+} + \partial_\eta{}^{+}A^{-} - Re^{-1}\ \partial_\eta J^{-1} N]\Delta Q^{*} = -RHS \tag{48}$$

$$[\frac{I}{J\Delta t} + \partial_\zeta{}^{-}\ B^{+} + \partial_\zeta{}^{+}B^{-} - Re^{-1}\ \partial_\zeta J^{-1} M]\Delta Q = \frac{\Delta Q^{*}}{J\Delta t} \tag{49}$$

$$RHS = \partial_\eta{}^{-}G^{+} + \partial_\eta{}^{+}\ G^{-} + \partial_\zeta{}^{-}H^{+} + \partial_\zeta{}^{+}H^{-} - Re^{-1}\{\partial_\eta[J^{-1}(\eta_x R + \eta_y S)] + \partial_\zeta[J^{-1}(\zeta_x R + \zeta_y S)]\} \tag{50}$$

The (+) and (-) superscripts indicate flux split quantities, according to the flux vector splittings of Van Leer. A and B are linearizations of the G and H fluxes, and M and N arise from the linearizations of viscous terms in the ζ - direction and η - direction, respectively. All viscous terms are centrally differenced, and implicit cross-derivative terms are neglected in the formulation.

A comparative study of these two schemes is to be reported in Ref. 24.

4. RESULTS AND DISCUSSION

Two Navier-Stokes codes are developed as the tools of analysis. Both codes are second order accurate in time and in space. Code A is the explicit and time unsplit MacCormack scheme, which proves its use from straightforward vectorization point of view (Ref. 21). Code B is an implicit fully-upwind line-Gauss-Seidel relaxation scheme that necessitates flux-vector splitting (Ref. 22). For a class of unsteady flows, the explicit scheme may be more computer-time efficient. However, despite its parallelization complications due to recursiveness, the implicit scheme is much faster converging for steady flows, thence often preferred.

In an attempt to demonstrate the integrity of these schemes for various flow dynamics phenomena and perform comparisons, a variety of high-Reynolds-number flow cases are analyzed. These include flow over a flat over a flat plate with a leading edge (Fig. 5), flow over a sharp concave corner (Fig. 6), and flow over a rearward facing step (Fig. 7). Among the phenomena observed through simulation are, initiation and growth of a boundary layer, shock-boundary layer, shock-boundary layer interaction, expansion around a ninety-degree corner and separation, and detached shock.

The flow simulations are performed using CDC VPS-32 vector processor

which has a virtual memory architecture. This memory-to-memory machine has short stops which does not use vector registers. For this SIMD (single-instruction-multiple-data) processing, the user has to do the memory management and prescribe the required resources, such as, the working set sizes, to the operating system. Page memories used by the code are not necessarily adjacent, therefore, vector lengths larger than a page (64K-words) are avoided. Thirty-two bit (half-precision) arithmetic option and very efficient scatter-gather operations are available, therefore, they are widely used in this code development. The vectors shorter in length than the breakeven length are retained in scalar DO loops. The array indeces are arranged in decreasing lengths and the nested DO loops containing these indeces are ordered likewise, so that, the innermost loop corresponds to the longest dimension. Avoidable uses of vector logical unit are eliminated.

The implicit scheme poses the recurrence problem from parallelization standpoint. Most of the operations of the inversion, however, occurs in the LU decomposition for four by four block line inversions, and they can be computed simultaneously for all the lines before beginning the relaxation sweeps. The Gauss-Seidel line inversions constitute less than thirty percent of total computations as indicated by the histograms (approximately 23% in turbulent and 26% in laminar calculations). Therefore, a further improvement in computation times would have been achieved by employing a parallel algorithm. The scalar computational time on VPS-32 for the above algorithm is approximately 800 microseconds per gridpoint per time step. This vectorized upwind scheme achieves a speed up to approximately 17 microseconds per gridpoint per time step for laminar Navier Stokes calculations and 21 microseconds for turbulent Navier Stokes calculations. Another 21% time reduction can be obtained if thin-layer Navier Stokes equations are

used. The scaler computation time for the MacCormack code, 240 microseconds per grid point per time step, is reduced to 40 microseconds through vectorization. Better speed-ups are possible for larger mesh sizes.

Further discussion on computational methodology comparisons are discussed in Ref. 24. This reference also includes analyses and simulations for flow over an airfoil and flow over an ogive-nosed cylinder at angles of attack. Such cases are of interest to the second part of this investigation, therefore, not included in this report.

Two-dimensional simulations of cavity flowfields are demonstrated in Figures 8 through 25. These results certainly do not reflect the third-dimension effects of the side walls. The box-cavity flowfield is symmetrical with respect to its centerplane which is at z = width/z (Fig. 1). Two-dimensional simulations reflect the flowfield at this plane of symmetry. Example cases included are two open cavities (length-to-depth ratios are 3 and 6), a transitional cavity (length-to-depth ratio is 12), and two closed cavities (length-to-depth ratios are 16 and 24). Figures corresponding to these cases are 11 through 13, 14 through 16, 17 through 19, 20 through 22, and 23 through 25, respectively. All of these figures display the final property values at 0.1 seconds after the computations are intiated. These results are also reported in References 16 through 18, which are authored or co-authored by the principal investigator of this research.

5. CONCLUDING REMARKS

An explicit-implicit and an implicit two-dimensional Navier-Stokes code along with various grid generation capabilities are developed. A series of classical benchmark cases are simulated using these codes.

References 16, 17, 18, and 24. Current follow-up efforts may be summed up as; developing explicit as well as implicit three dimensional codes, three-dimensional cavity flowfield studies and simulations, two-dimensional and three-dimensional store flowfield studies and simulations.

REFERENCES

1. Stallings, R. L., Jr., "Store Separation from Cavities at Supersonic Flight Speeds," Journal of Spacecraft and Rockets, Vol. 20, No. 2, pp. 129-132, 1983.

2. Blair, A. B. and Stallings, R. L., "Supersonic Axial-Force Characteristics of a Rectangular-Box Cavity with Various Length-to-Depth Ratios in a Flat Plate," NASA-TM-87659, April 1986.

3. Rossiter, J. E., "Wind Tunnel Experiment on the Flow Over Rectangular Cavities at Subsonic and Transonic Speeds," R&M No. 3438, British A.R.C., October 1964.

4. Charwat, A. F., Rous, J. N., Dewey, F. C., and Hitz, J. A., "An Investigation of Separated Flows," J. of Aerospace Sciences, vol. 28 Part I, June 1961, Part II, July 1961.

5. McDearmon, R. W., "Investigation of the Flow in a Rectangular Cavity in a Flat Plate at a Mach Number of 3.55," NASA TN D-523, September 1960.

6. McGregor, O. W., and White, R. A., "Drag of Rectangular Cavities in Supersonic and Transonic Flow Including the Effects of Cavity Resonance, "AIAA Journal, vol. 8, November 1970.

7. Sinha, S. N., Gupta, A. K., Oberai, M. M., "Laminar Separating Flow Over Backsteps and Cavities," AIAA Journal, Vol. 20, No. 3, 1982.

8. Antonov, A. N. and Shalaev, S. P., "Experimental Investigation of Nonstationary Flow in Cavities in a Supersonic Flow," Fluid Dynamics-Soviet Research, vol. 14, no. 5, 1980.

9. Varfolomeyev, I. M., Gortysher, Y. F. and Shekukin, V. K., "Heat Transfer and Dynamics of Supersonic Airflow Past Cavities," Heat Transfer-Soviet Research, vol. 13, 1981.

10. Clark, R. L., Kaufman, L. G., Maciulaitis, A., "Aeroacoustic Measurements for Mach 0.6 to 3.0 Flows Past Rectangular Cavities," AIAA Paper No. 80-0036, 1980.

11. Borland, C. J., "Numerical Prediction of the Unsteady Flowfield in an Open Cavity," AIAA Paper No. 79-0136, 1979.

12. Hankey, W. L.; and Shang, J. S., "Numerical Solution to Pressure Oscillations in an Open Cavity," AIAA Paper No. 79-0136, 1979.

13. Gatski, T. B. and Grosch, C. E., "Embedded Cavity Drag in Steady Laminar Flow," AIAA Journal, Vol. 23, No. 7, 1985.

14. Gorski, J. J. and Chakravarthy, S. R., "Calculation of Three Dimensional Cavity Flowfields," AIAA Paper No. 87-0117, 1987 (to be presented).

15. Om, D., "Navier-Stokes Simulation for Flow Past an Open Cavity," AIAA Paper No. 86-2628, 1986.

16. Baysal, O., Stallings, R. L., Srinivasan, S., "Unsteady Flow in a Cavity at Supersonic Speeds and its Navier-Stokes Prediction with a Vectorized Algorithm," AIAA Paper No. 86-0594, 1986.

17. Baysal, O., Stallings, R. L., and Srinivasan, S., "Cavity Flowfield Calculations," Virginia Journal of Science, vol. 37, no. 2, p. 39, Summer 1986.

18. Baysal, O., Stallings, R. L., "Computational and Experimental Investigation of Cavity Flowfields," AIAA Paper No. 87-0114, January 1987 (to be presented).

19. Sindir, M. M. S., "A Numerical Study of Turbulent Flows in Backward Facing Step Geometries," Ph.D. Thesis, University of California, Davis, 1982.

20. Baldwin, B. S. and Lomax, H., "Thin Layer Approximations and Algebraic Model for Separated Turbulent Flows," AIAA Paper No. 78-257, 1978.

21. MacCormack, R. W., "Current Status of Numerical Solutions of the Navier-Stokes Equations," AIAA Paper 85-0032, 1985.

22. Thomas, J. L. and Walters, R. W., Upwind Relaxation Algorithms for the Navier-Stokes Equations. AIAA Paper No. 85-1501 CP, July 1985.

23. Rumsey, C. L., Thomas, J. L., Warren, G. P., and Liu, G. C.,, "Upwind Navier-Stokes Solutions for Separated Periodic Flows," AIAA Paper No. 86-0247, 1986.

24. Baysal, O., "Flow Simulations Using Upwind Line-Gauss-Seidel and MacCormack Schemes On a Vector Processor," 1987 ASME Fluids Engineering Conference, Cincinnati, Ohio, June 1987 (to be presented).

25. Carter, J. E., "Numerical Solutions of the Navier-Stokes Equations for the Supersonic Laminar Flow Over a Two-Dimensional Compression Corner," NASA-TR-R385, July 1972.

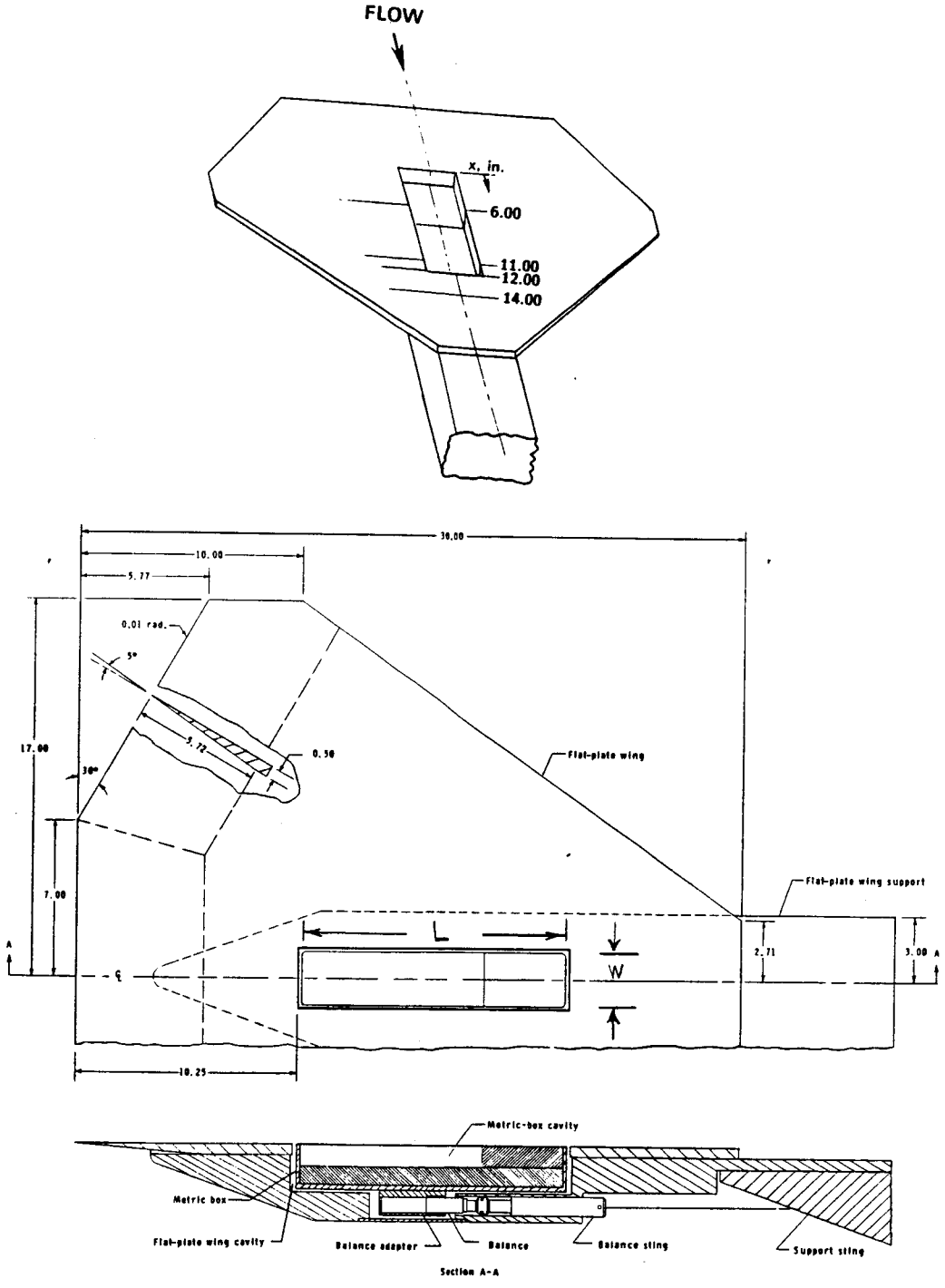

Figure 1. Details of flat plate wing metric-box-cavity from Ref. 2.

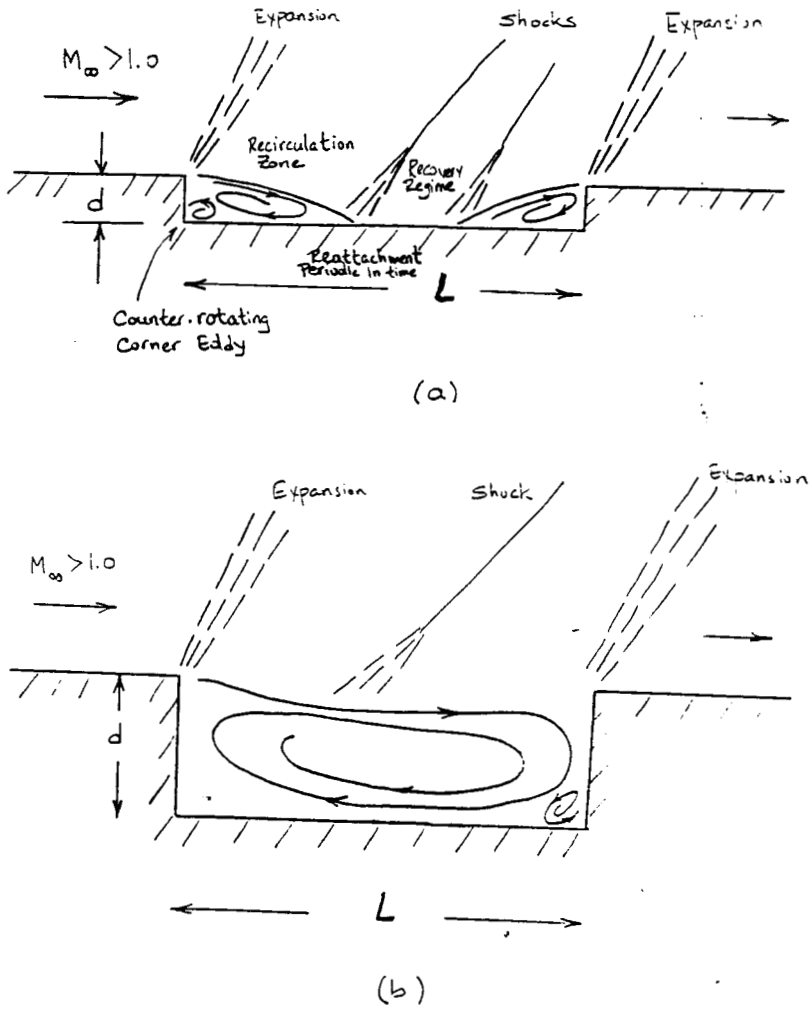

Figure 2. Hypothetical structure of flowfield variation due to depth-to-length ratio: (a) Closed or shallow cavity, (b) open or deep cavity.

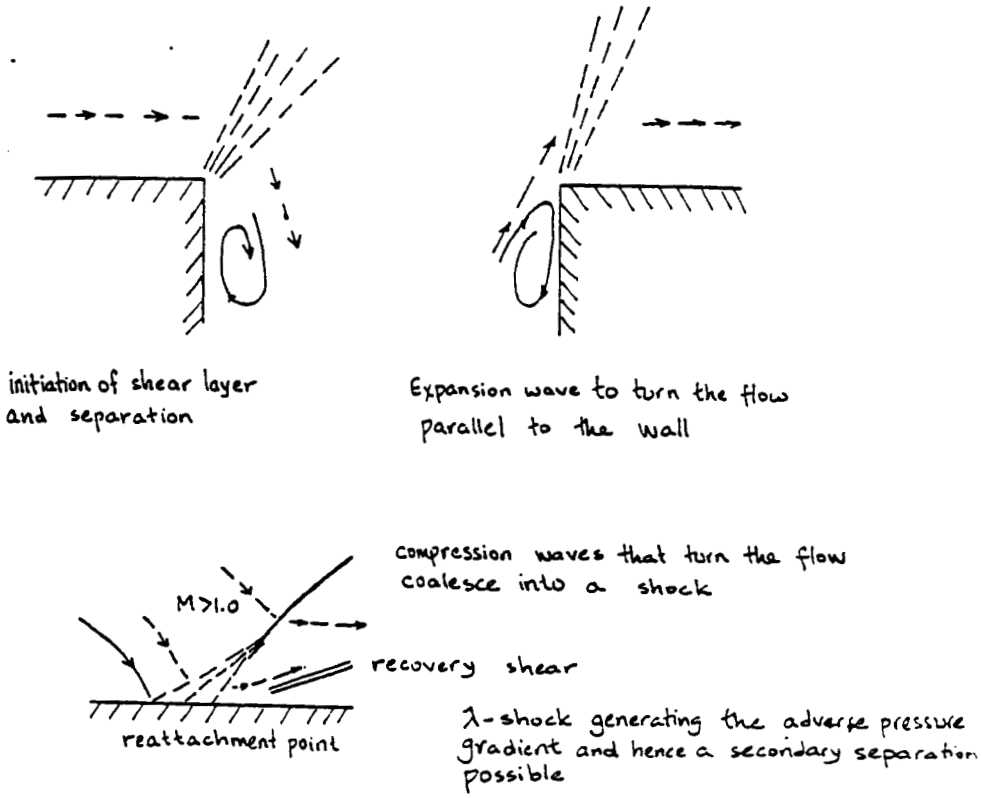

Figure 3. Hypothetical details of flowfield structure at cavity corners and cavity floor.

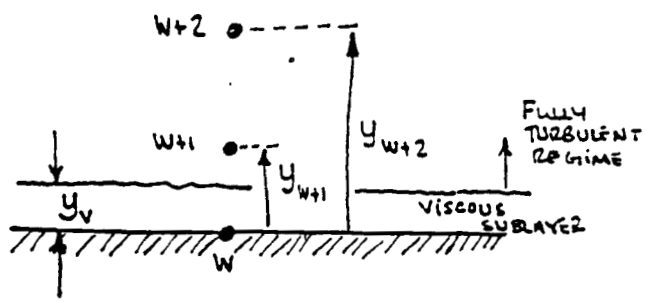

Figure 4. Near-wall region for low-Reynolds-number k-ε calculations or wall functions.

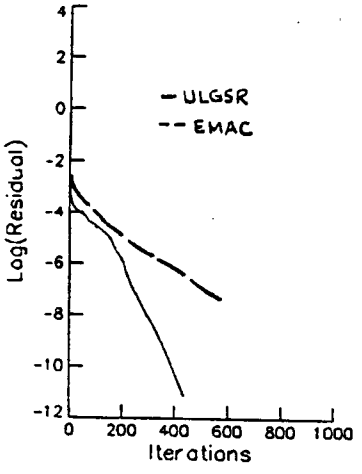

(a)

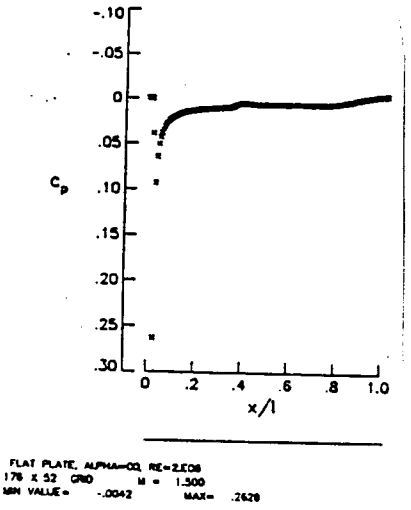

(b)

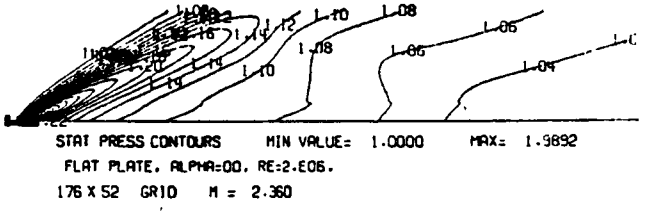

(c)

(d)

Figure 5. continued

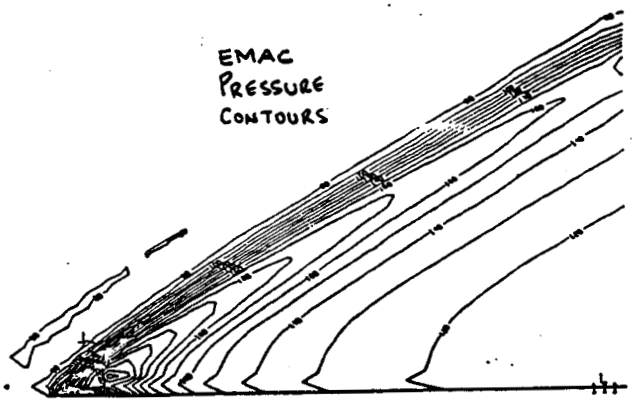

(e)

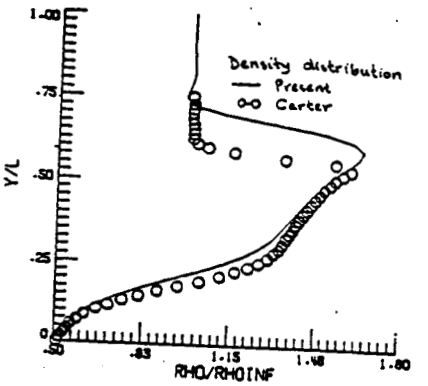

(g)

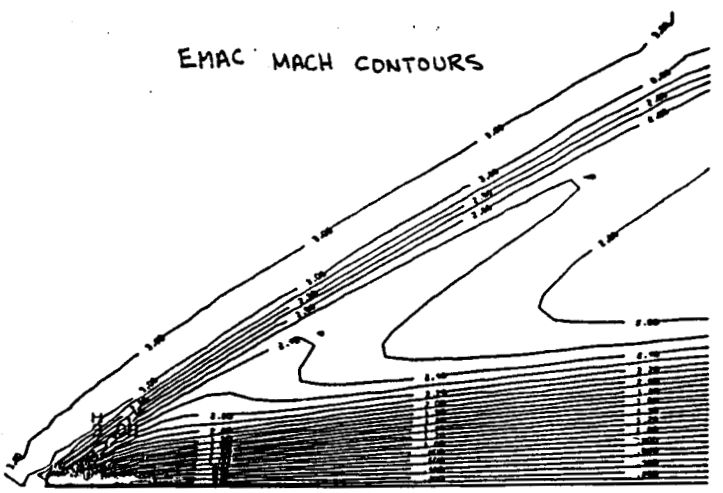

(f)

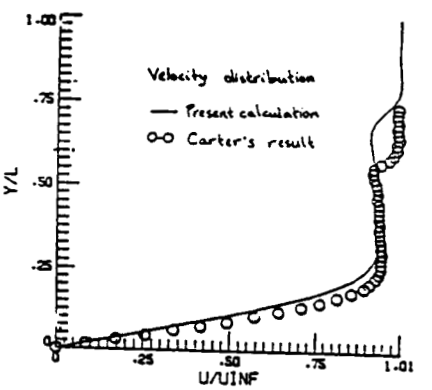

(h)

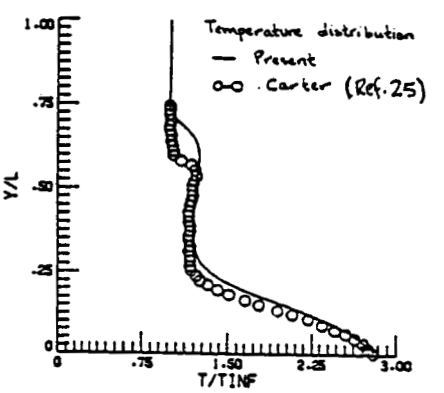

(i)

Figure 5. Supersonic flow over a flat plate with a leading edge: (a) convergence comparison of EMAC and ULGSR codes, (b-d) sample results by ULGSR code, (e-i) sample results by EMAC code.

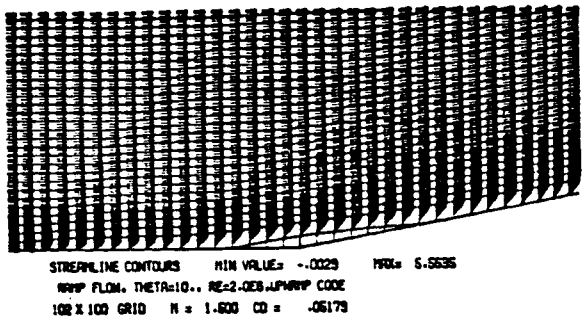

(a)

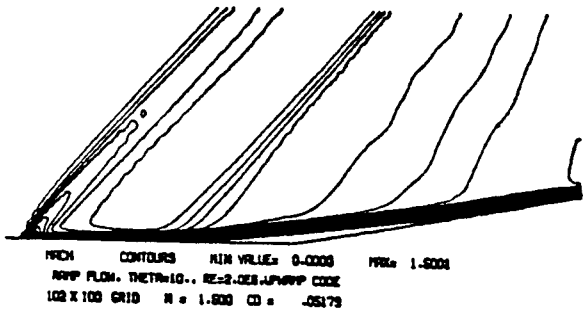

(b)

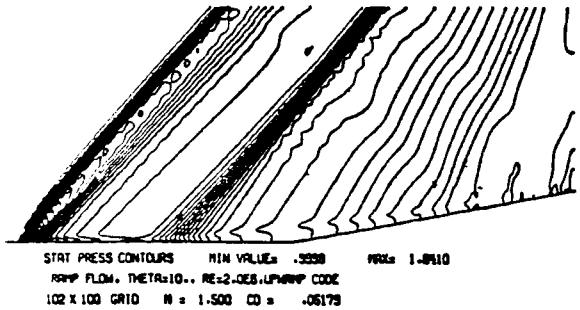

(c)

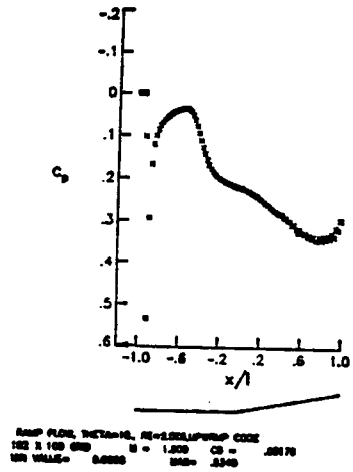

(d)

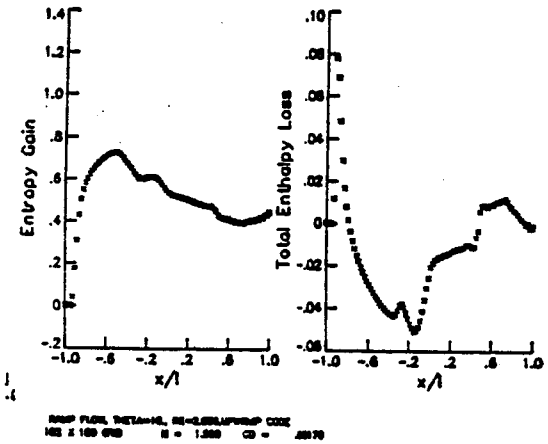

(f) (g)

Figure 6. continued

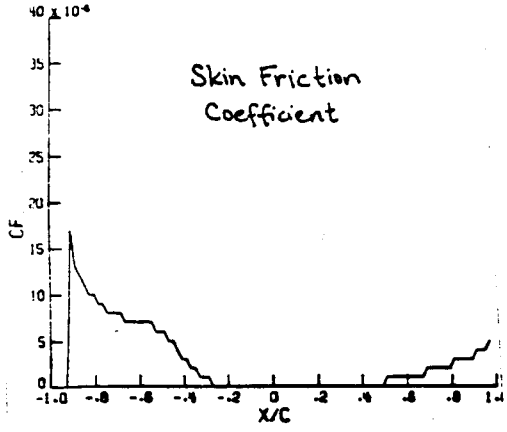

(h)

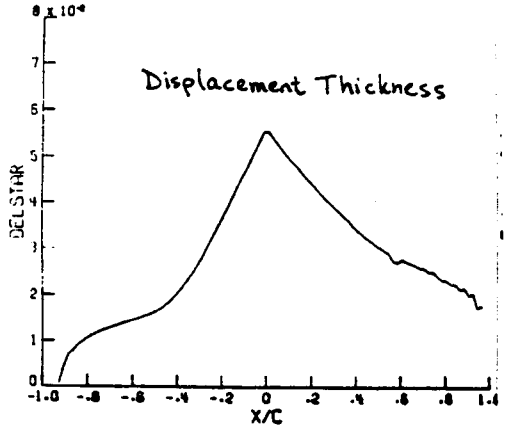

(i)

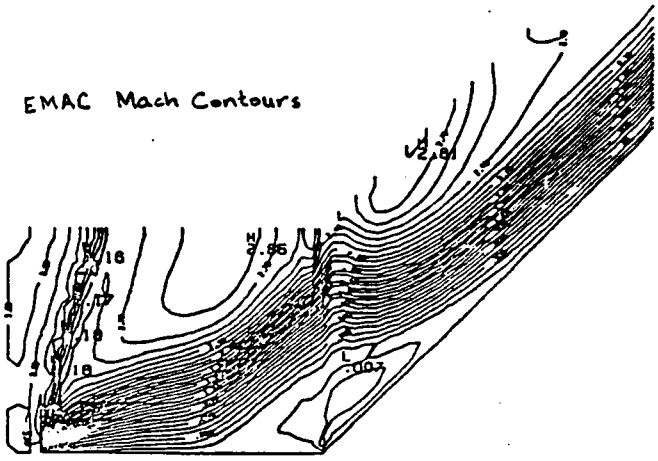

(j)

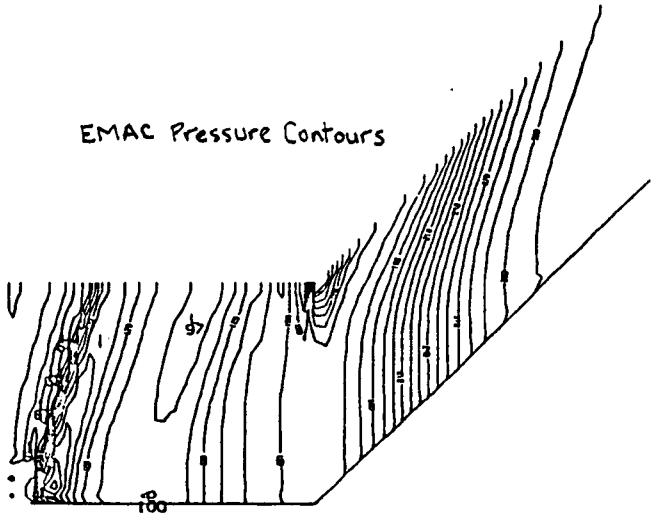

(k)

Figure 6. Supersonic flow over a 10°-Compression Corner: (a-i) ULGSR code, (j-k) EMAC code.

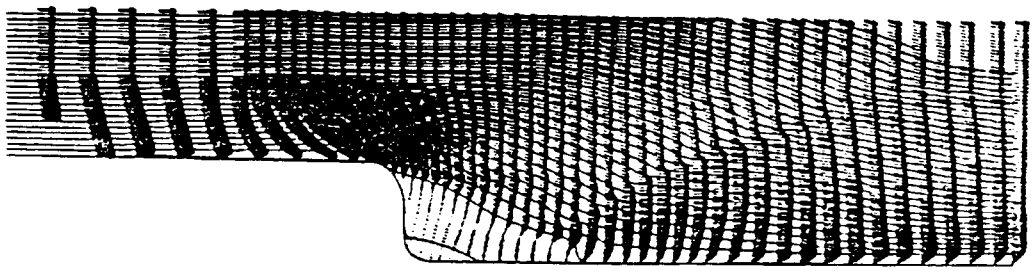

STREAMLINE CONTOURS MIN VALUE= -.0427 MAX= 3.0869
CAVITY FLOW.L/D=6.0. RE=2.0E6
97 X 90 GRID M = 1.500

(a)

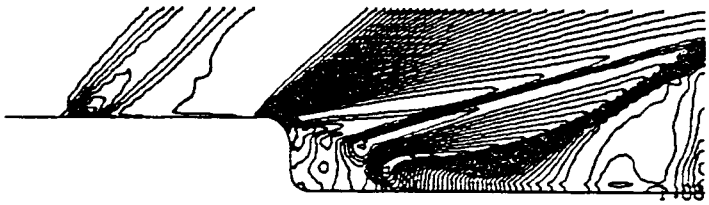

STAT PRESS CONTOURS MIN VALUE= .2546 MAX= 1.3105
STEP FLOW. L/D=INF. RE=2.0E6
97 X 90 GRID M = 1.500 CD = .37220

(b)

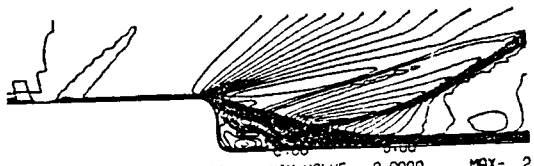

MACH CONTOURS MIN VALUE= 0.0000 MAX= 2.3770
STEP FLOW. L/D=INF. RE=2.0E6.
97 X 90 GRID M = 1.500 CD = .37220

(c)

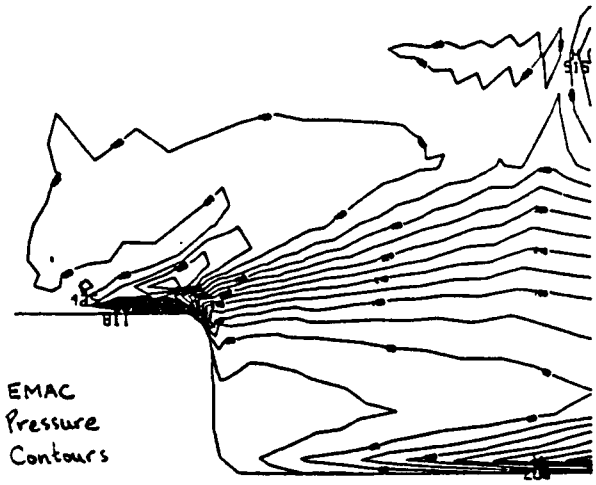

(d)

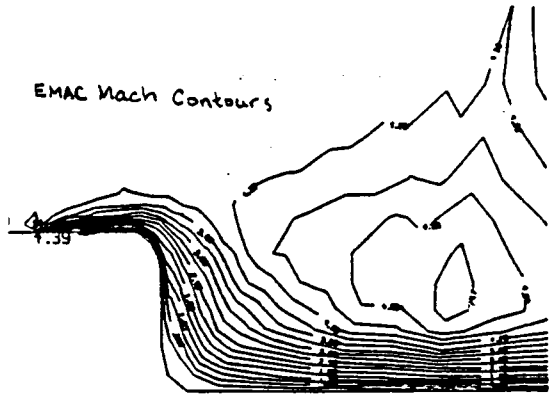

(e)

Figure 7. Supersonic flow over a rearward-facing step: (a-c) ULGSR code, (d-e) EMAC code.

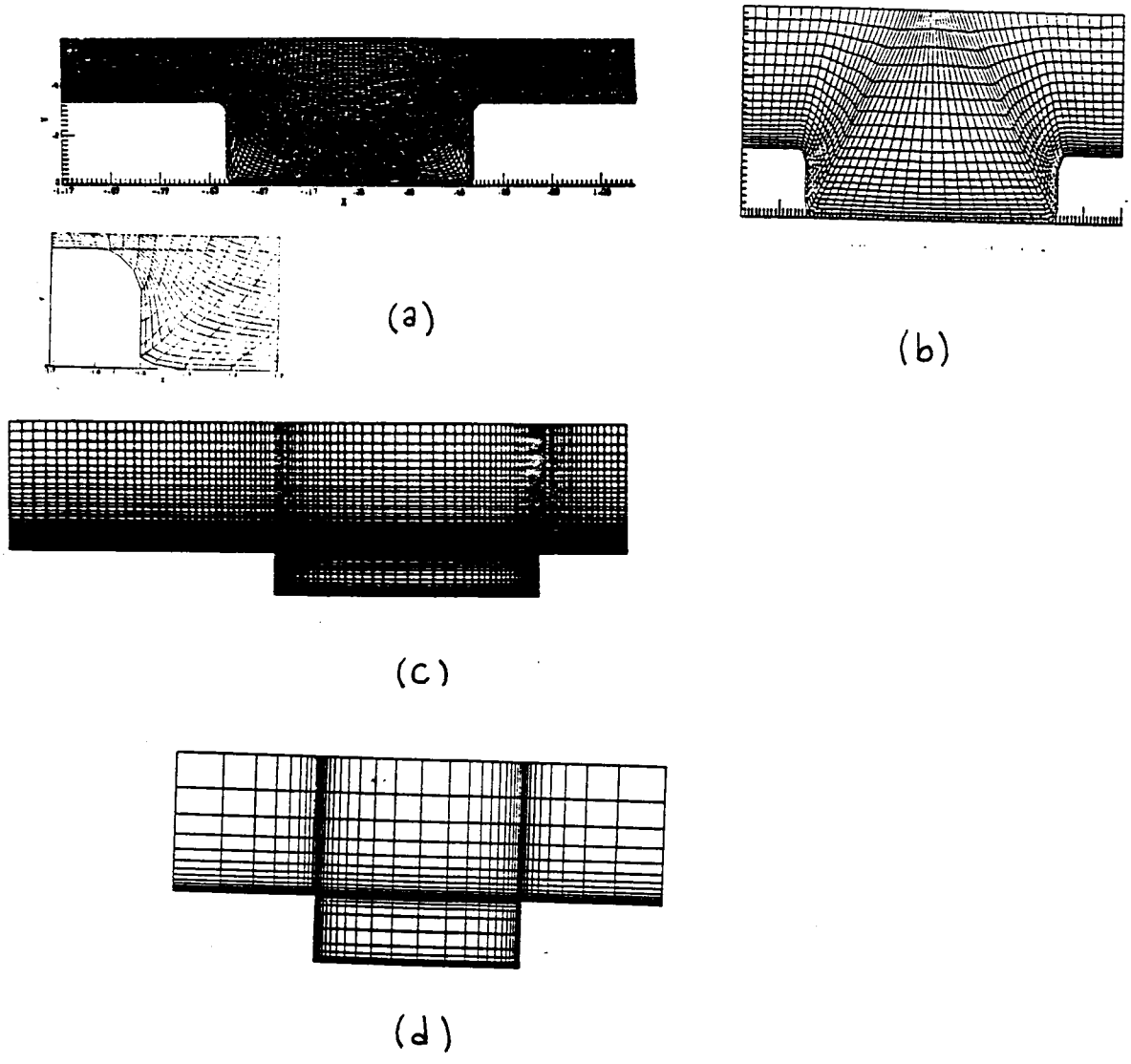

Figure 8. Sample grid meshes for cavity flowfield calculations: (a-b) body-fitted meshes, (c-d) patched rectangular meshes.

CAVITY FLOW FIELDS

OPEN CAVITY FLOW

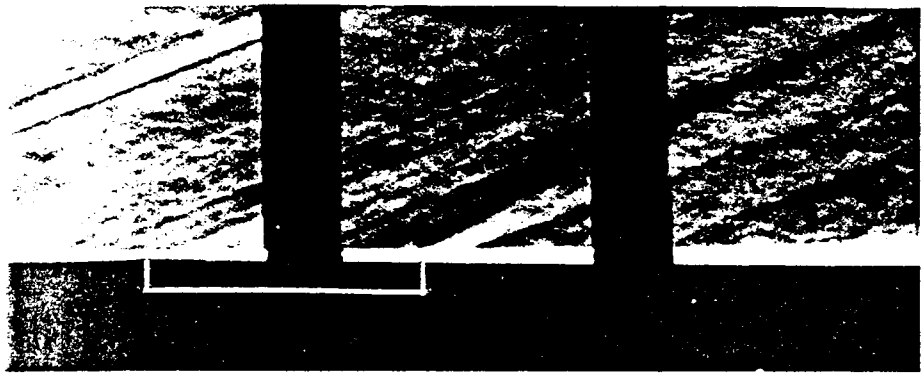

L/D = 11.2

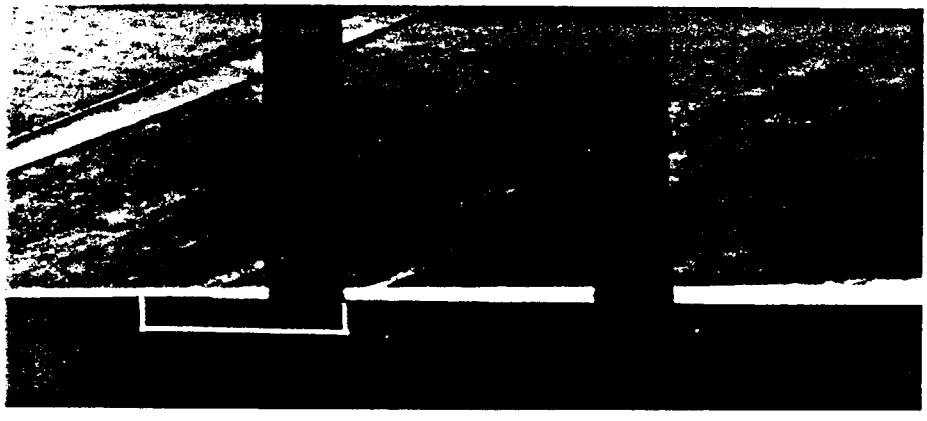

L/D = 8.0

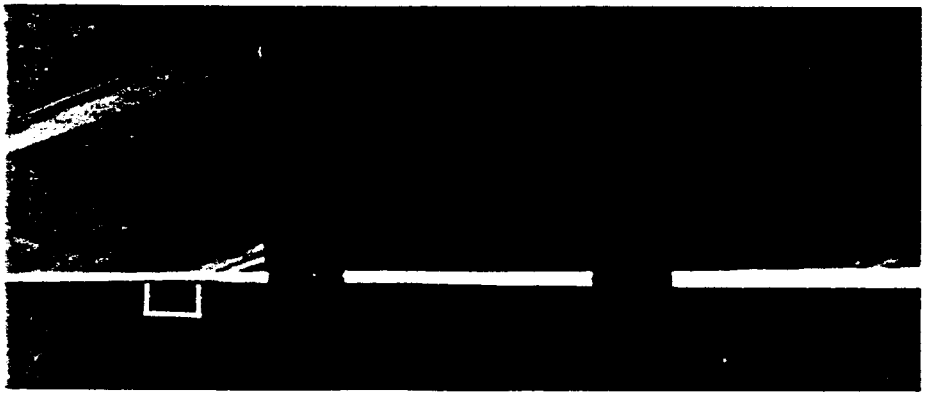

L/D = 2.0

Figure 9. Continued

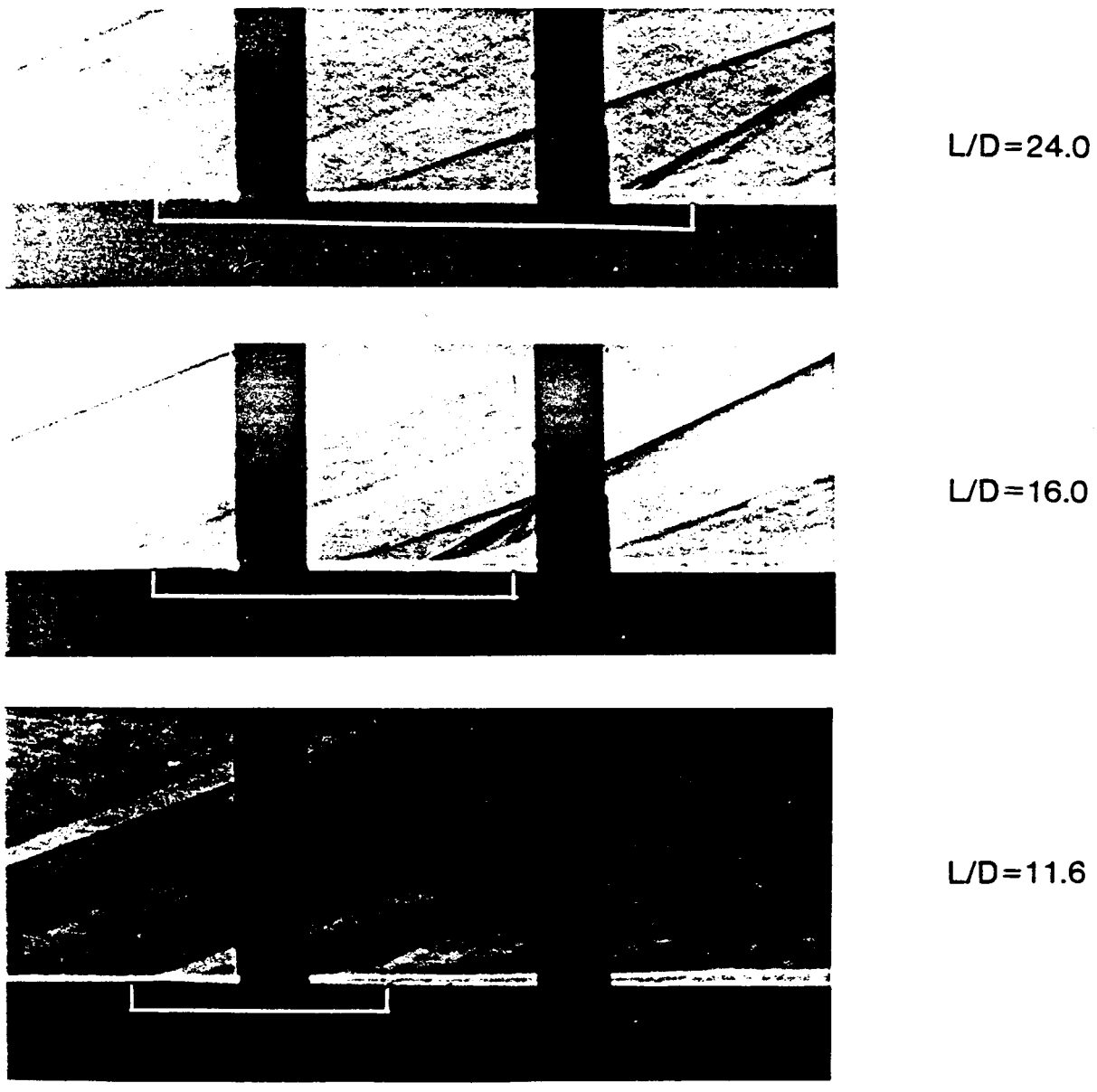

Figure 9. Schlieren photographs of cavity flowfields from Ref. 2: (a) Open cavity examples, (b) closed cavity examples.

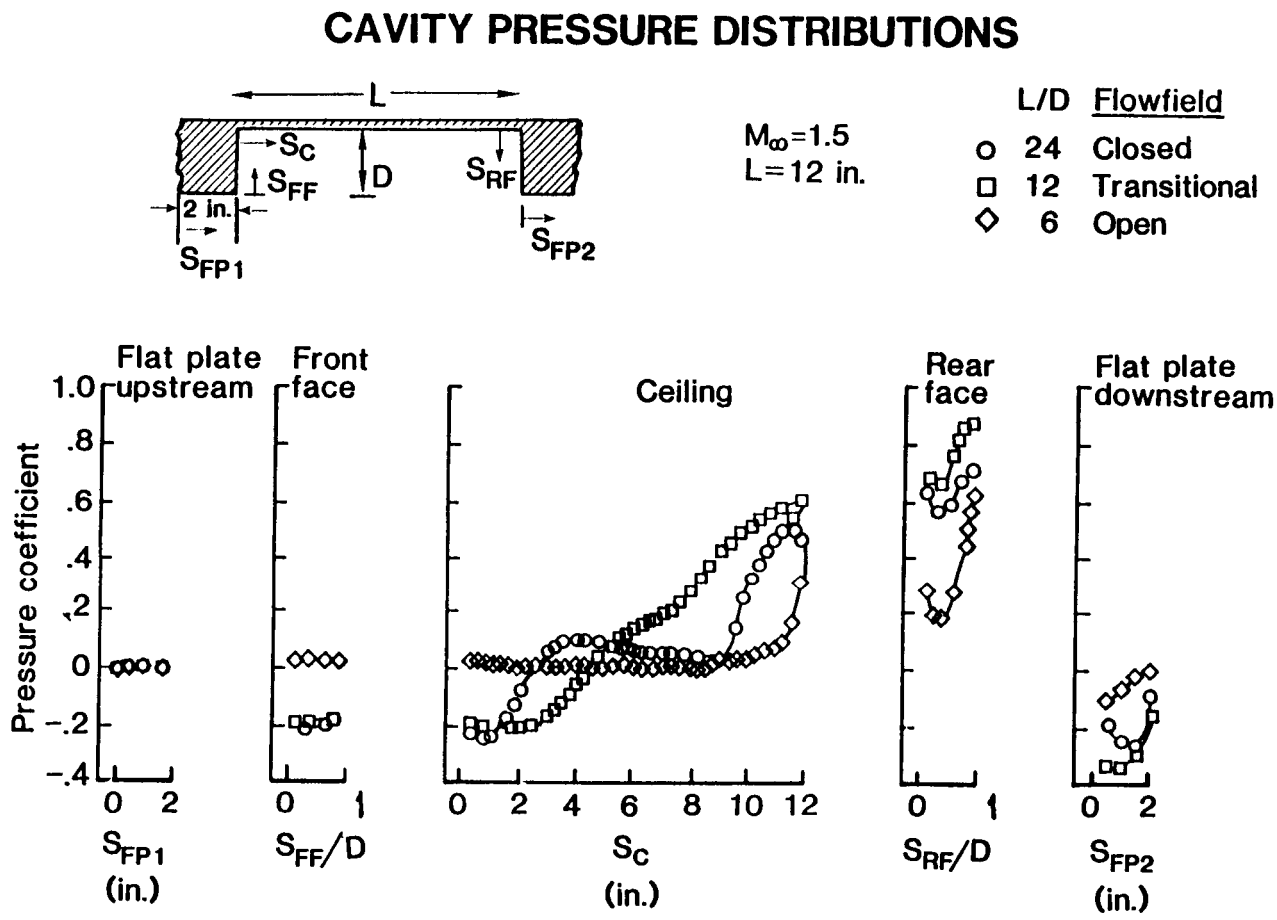

Figure 10. Experimentally determined pressure distributions of cavity flowfields from Ref. 2.

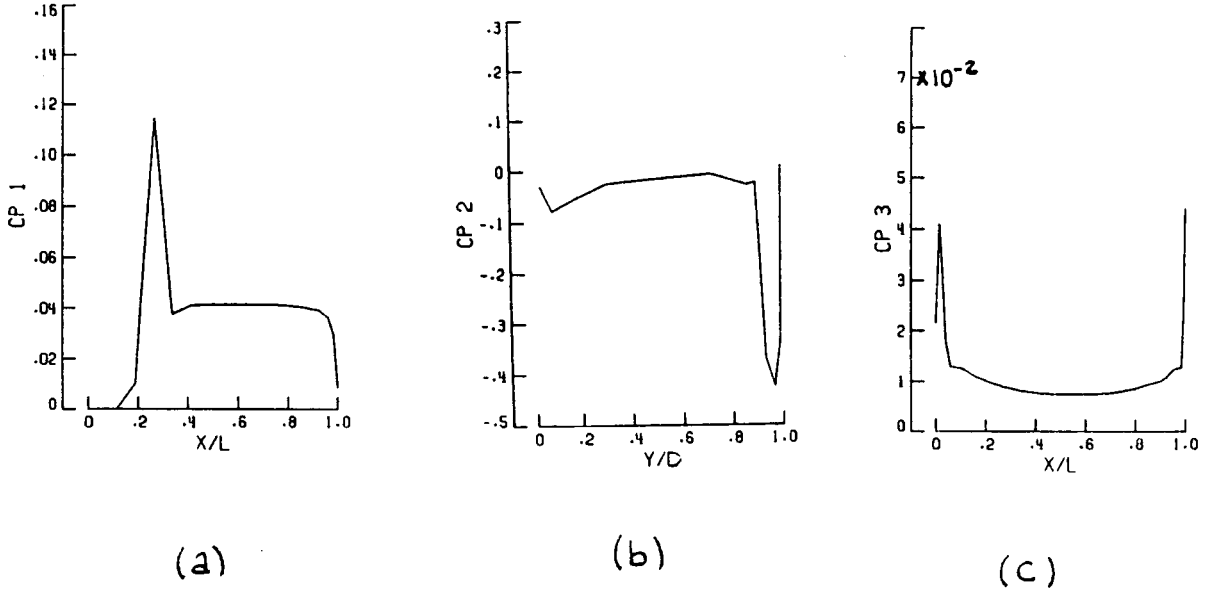

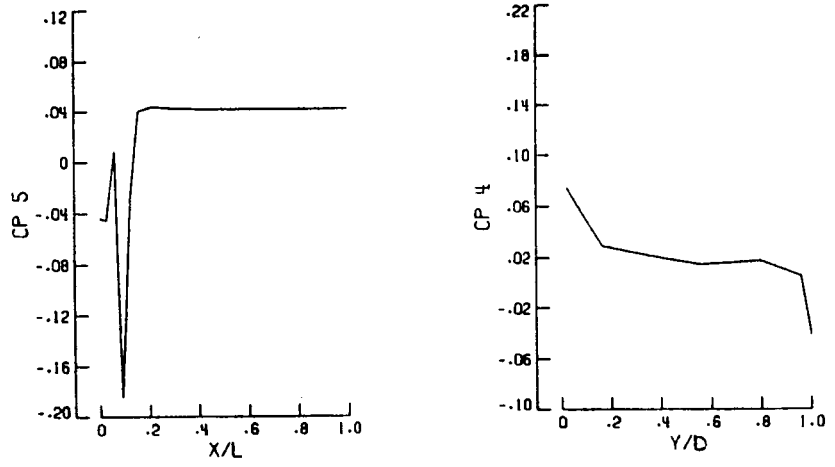

Figure 11. Continued

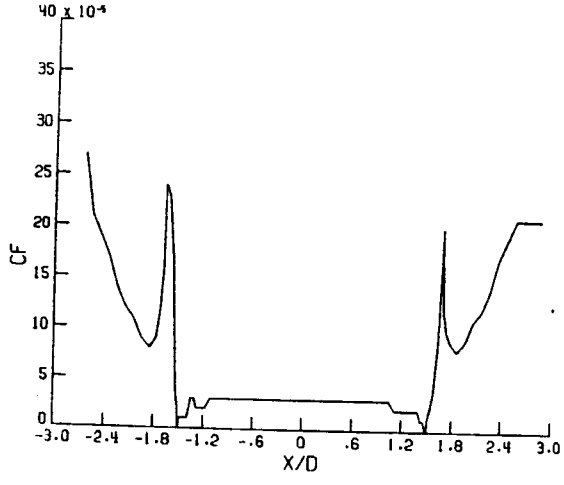

(f)

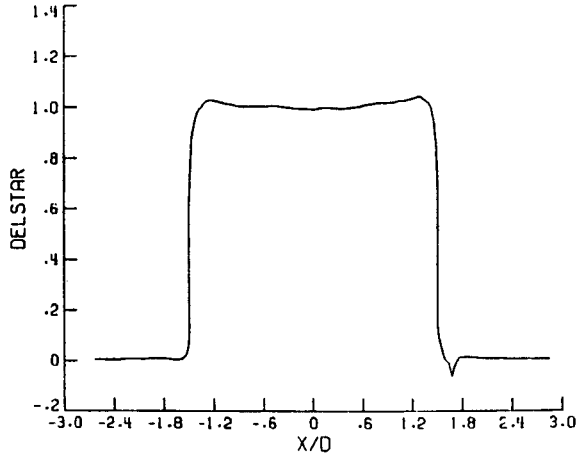

(g)

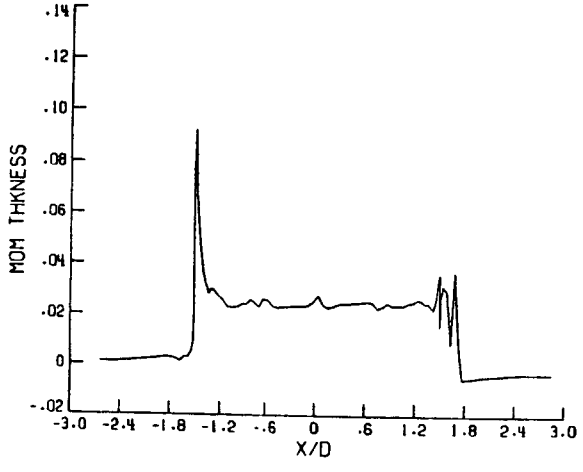

(h)

Figure 11. Supersonic flow over L/D = 3.0 cavity: Pressure coefficient distribution at, (a) front flat plate, S_{FP1}, (b) forward face, S_{FF}, (c) ceiling, S_C, (d) rearward face, S_{RF}, (e) rear flat plate, S_{FP2}, (f) skin friction coefficient, (g) displacement thickness, (h) momemtum thickness distributions.

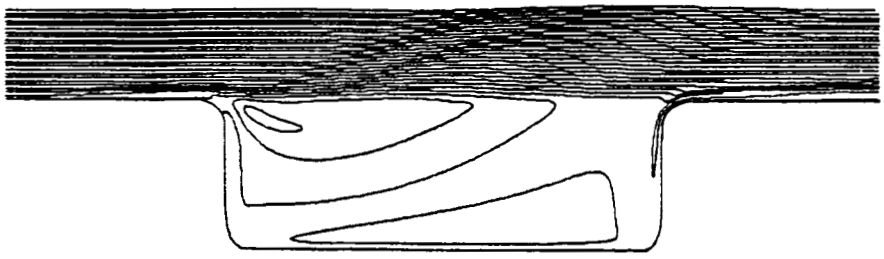

(a)

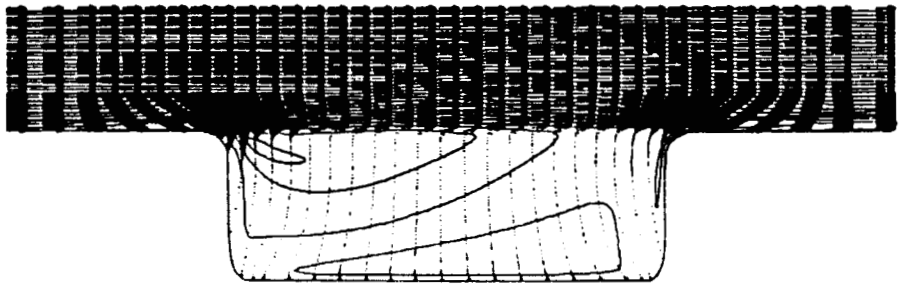

(b)

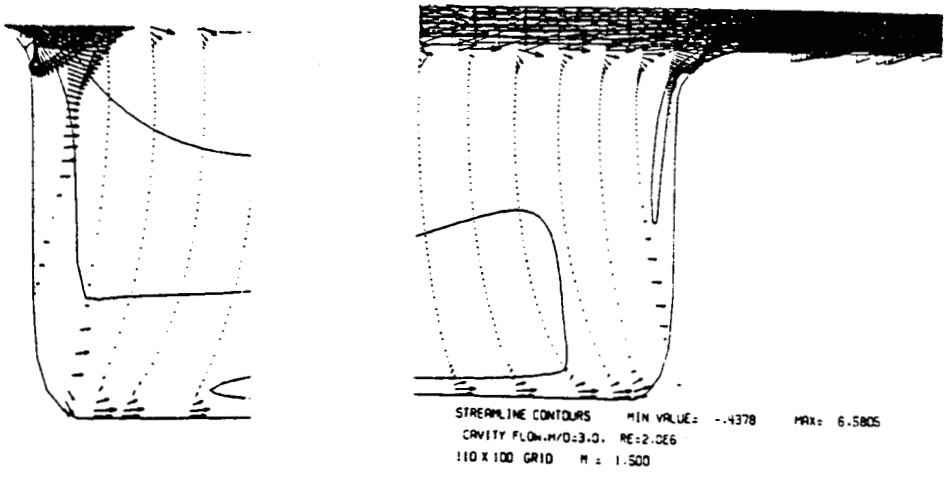

(c)

Figure 12. Supersonic flow over L/D = 3.0 cavity: (a) streamline contours, (b) velocity vectors of entire flowfield, (c) blow up of corner flows.

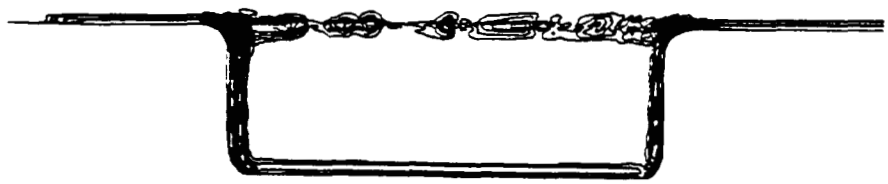

STAT PRESS CONTOURS MIN VALUE= .3084 MAX= 1.8617
CAVITY FLOW,H/D=3.0. RE=2.0E6
110 X 100 GRID M = 1.500

(a)

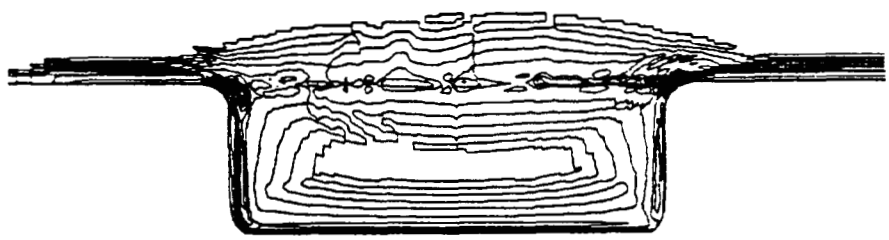

DENSITY CONTOURS MIN VALUE= .2828 MAX= 1.5987
CAVITY FLOW,H/D=3.0. RE=2.0E6
110 X 100 GRID M = 1.500

(b)

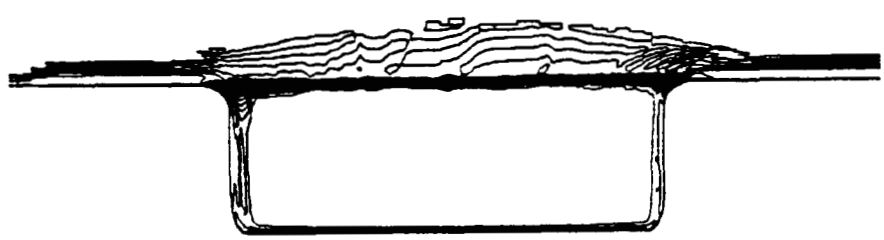

MACH CONTOURS MIN VALUE= 0.0000 MAX= 2.1188
CAVITY FLOW,H/D=3.0. RE=2.0E6
110 X 100 GRID M = 1.500

(C)

Figure 13. Supersonic flow over L/D = 3.0 cavity: (a) Pressure contours, (b) density contours, (c) Mach number contours.

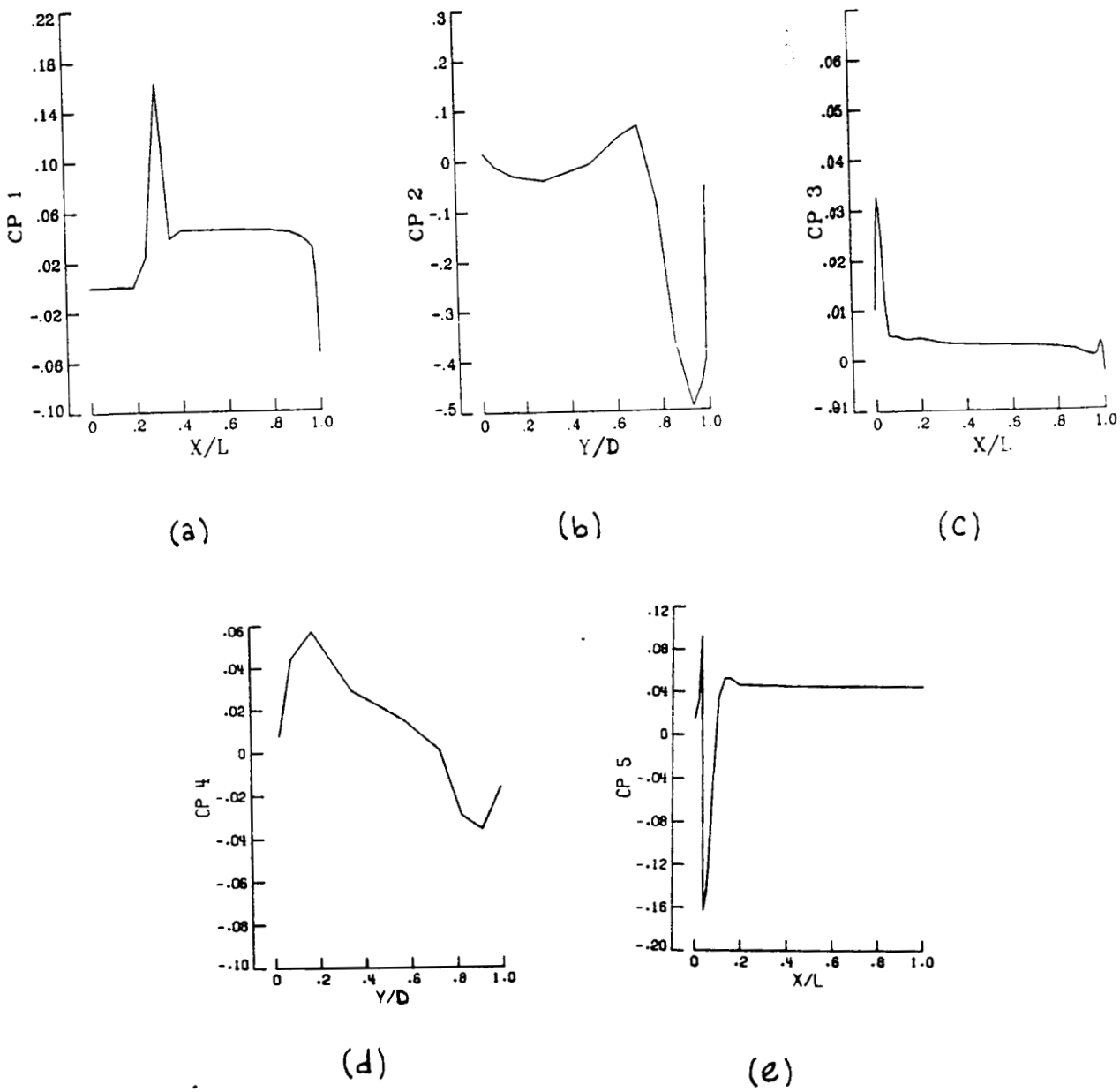

Figure 14. Supersonic flow over L/D = 6.0 cavity. Pressure coefficient distribution over; (a) front flat plate (S_{FP1}), (b) forward face (S_{FF}), (c) ceiling (S_C), (d) rearward-face (S_{RF}), and (e) rear flat plate (S_{FP2}). (See Fig. 10 for comparison).

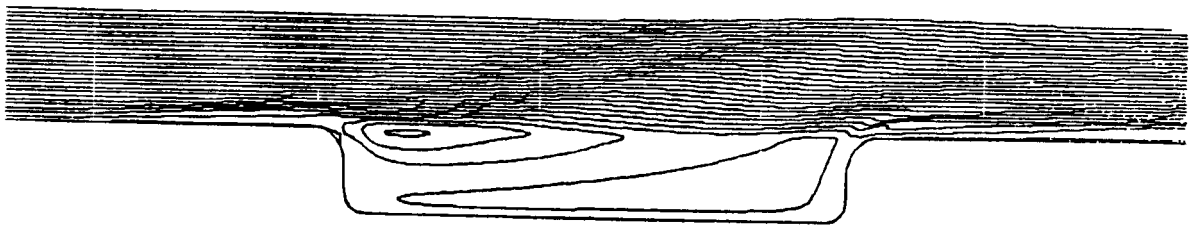

(a)

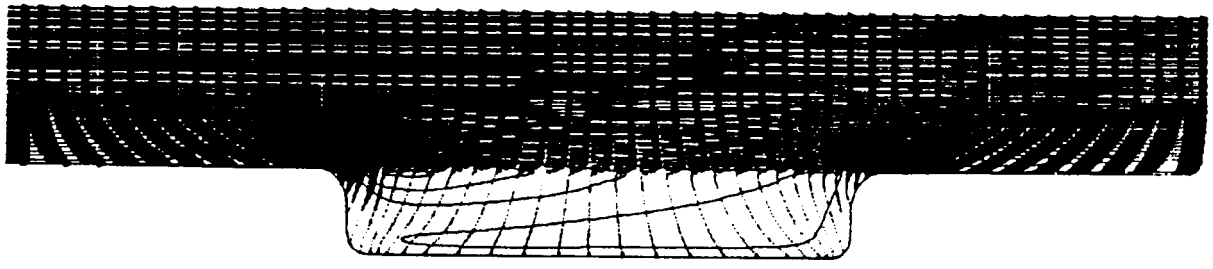

(b)

Figure 15. continued

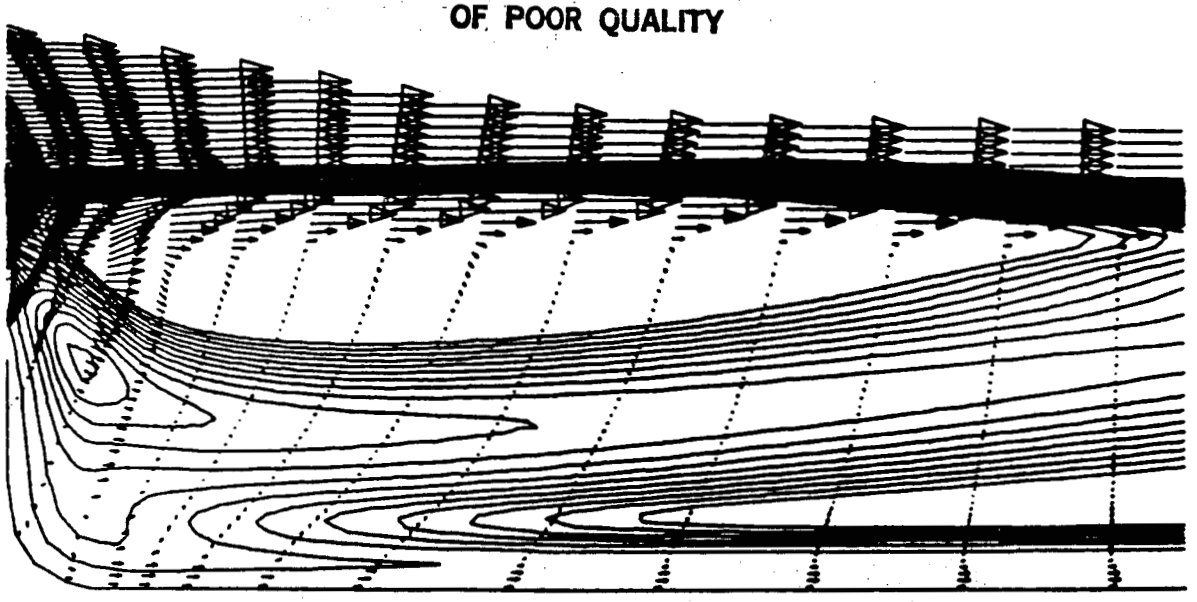

STREAMLINE CONTOURS MIN VALUE= -.1054 MAX= .3500
CAVITY FLOW.H/D=6.0. RE=2.0E6
M = 1.500

(c)

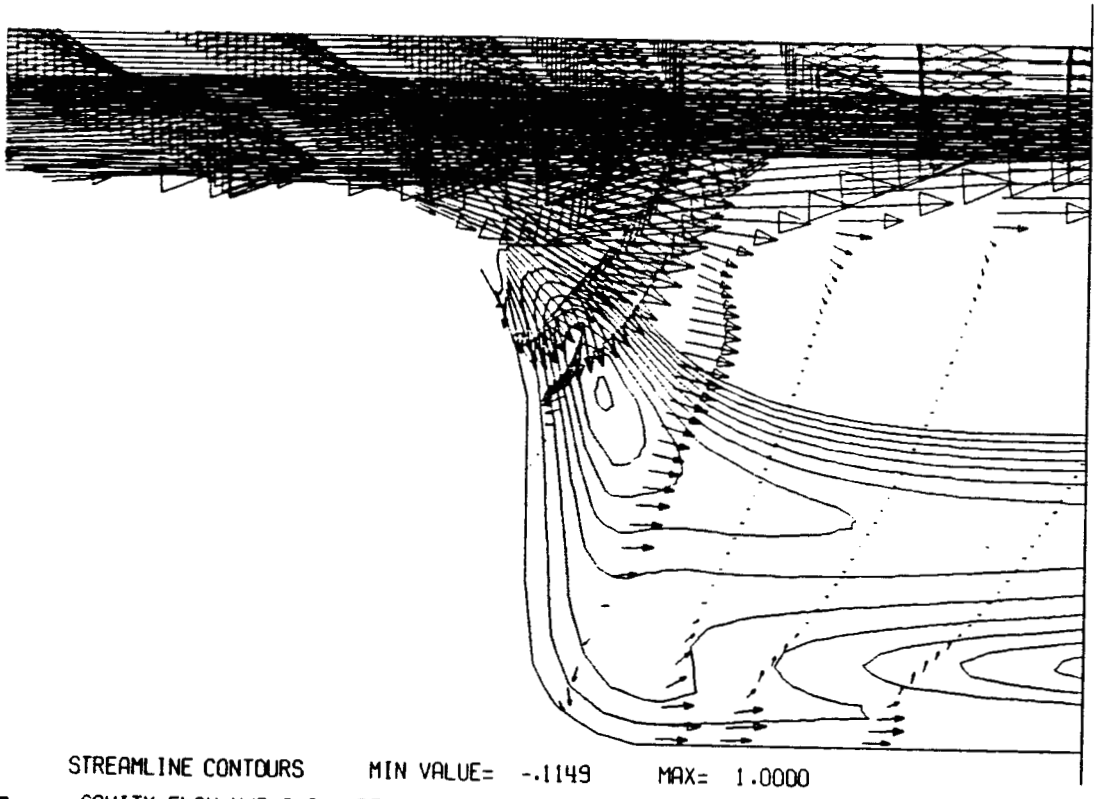

STREAMLINE CONTOURS MIN VALUE= -.1149 MAX= 1.0000
CAVITY FLOW.H/D=6.0. RE=2.0E6
110 X 100 GRID M = 1.500

(d)

Figure 15. continued

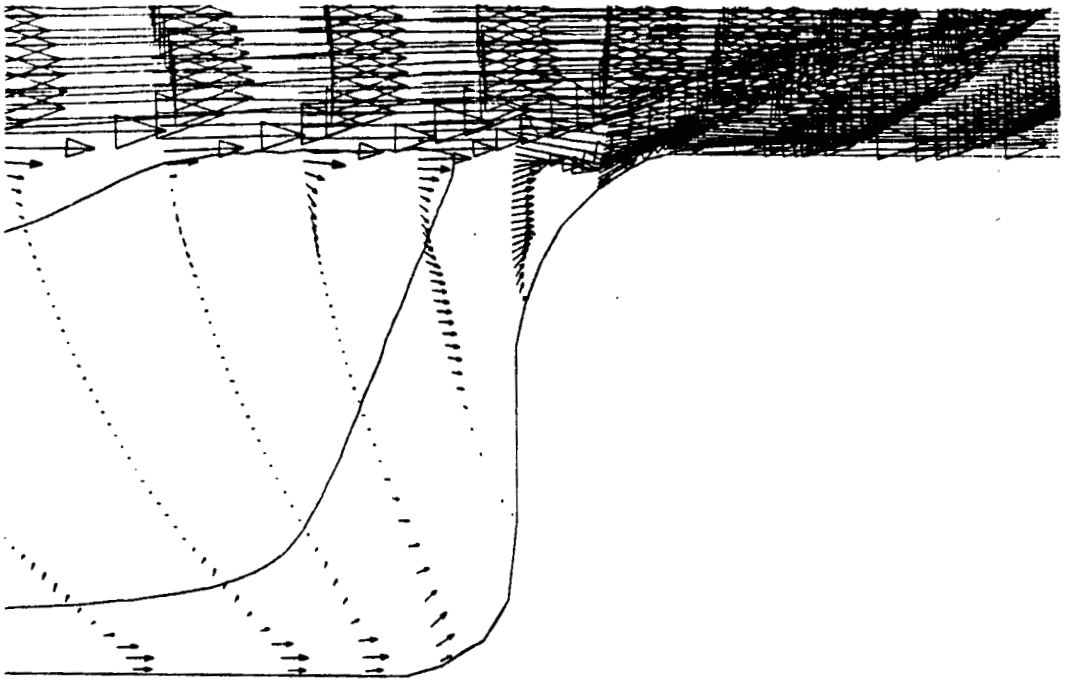

Figure 15. Supersonic flow over L/D = 6.0 cavity: (a) streamline contours, (b) velocity vectors, (c-e) blow ups, of corner flows.

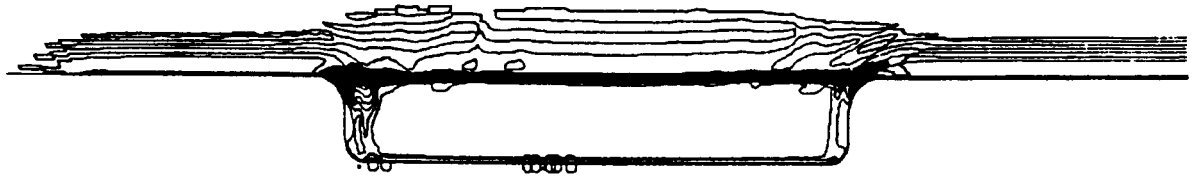

MACH CONTOURS MIN VALUE= 0.0000 MAX= 2.3786
CAVITY FLOW,H/D=6.0, RE=2.0E6
110 X 100 GRID M = 1.500

(a)

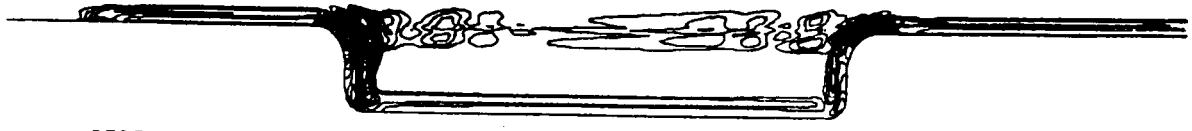

STAT PRESS CONTOURS MIN VALUE= .2236 MAX= 1.7688
CAVITY FLOW,H/D=6.0, RE=2.0E6
110 X 100 GRID M = 1.500

(b)

Figure 16. continued

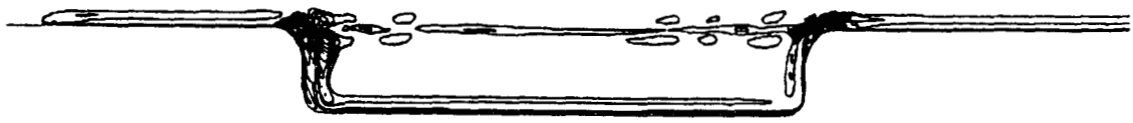

DENSITY CONTOURS MIN VALUE= .1994 MAX= 1.4821
CAVITY FLOW.H/D=6.0, RE=2.0E6
110 X 100 GRID M = 1.500

(c)

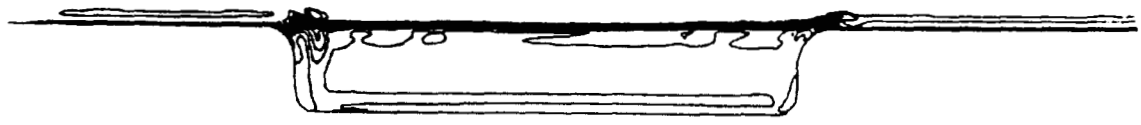

TOT P LOSS CONTOURS MIN VALUE= -.2594 MAX= .9391
CAVITY FLOW.H/D=6.0, RE=2.0E6
110 X 100 GRID M = 1.500

(d)

Figure 16. Supersonic flow over L/D = 6.0 cavity: (a) Mach number contours, (b) Pressure contours, (c) Density contours, and (d) total pressure loss contours.

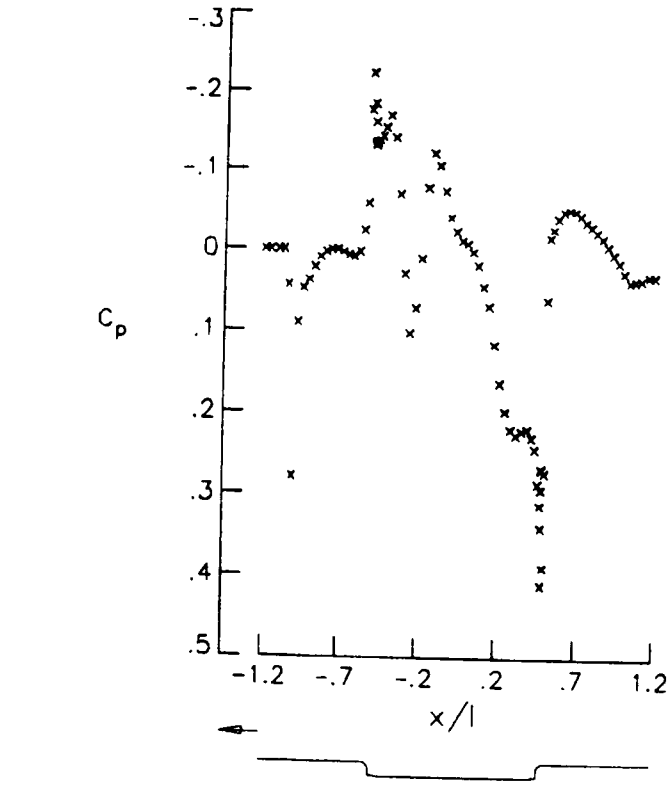

CAVITY FLOW,L/D=12.0, RE=2.0E6,
90 X 70 GRID M = 1.500
MIN VALUE= -.2233 MAX= .4103

(a)

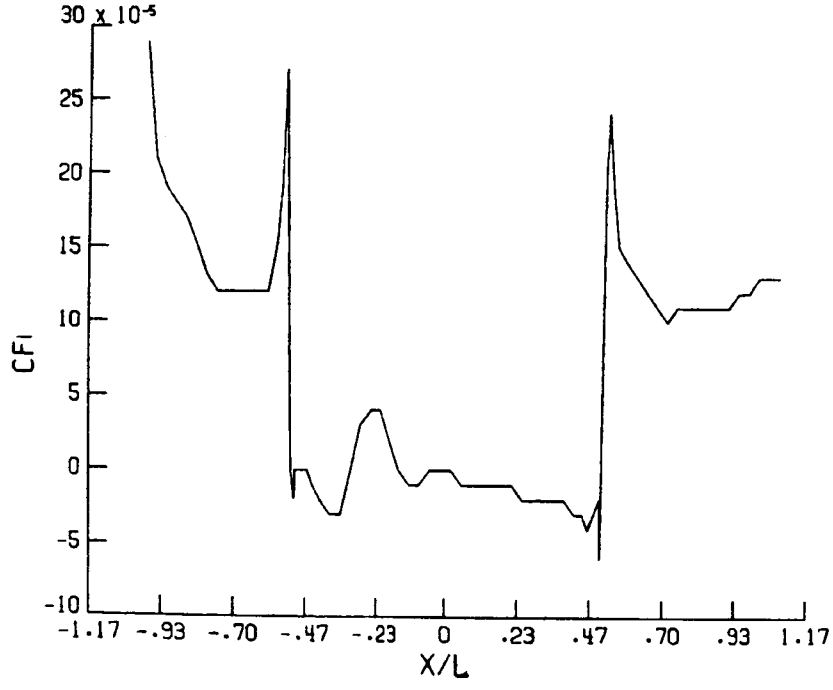

(b)

Figure 17. continued

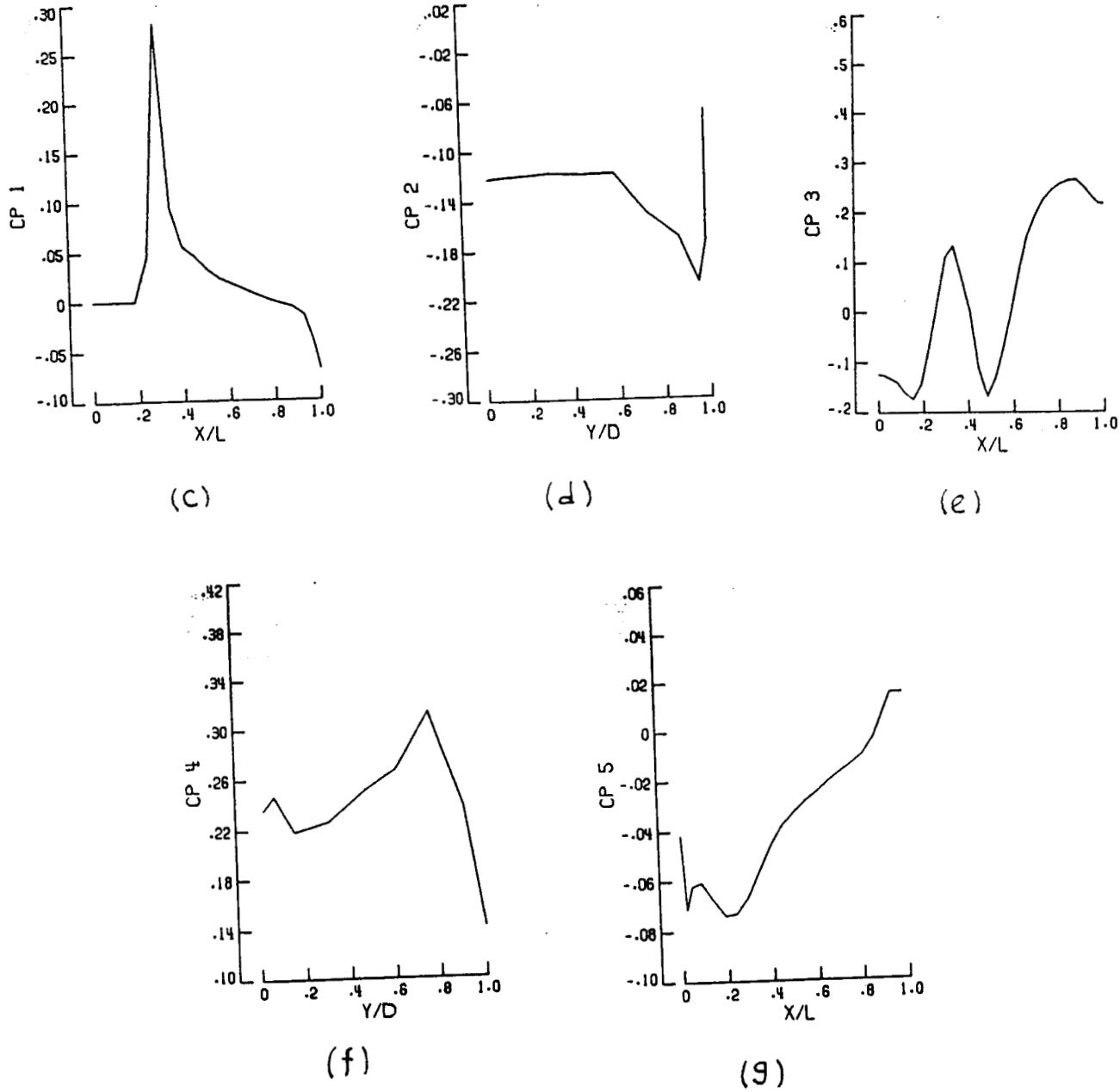

Figure 17. Supersonic flow over L/O = 12.0 cavity: (a) pressure coefficient distribution over entire wall, (b) skin friction coefficient distribution over entire wall, (c-g) pressure coefficient distribution on front flat plate (S_{FP1}), forward face (S_{FF}), ceiling (S_C), rearward face (S_{RF}), rear flat plate (S_{FP2}), respectively (see Fig. 10 for comparison).

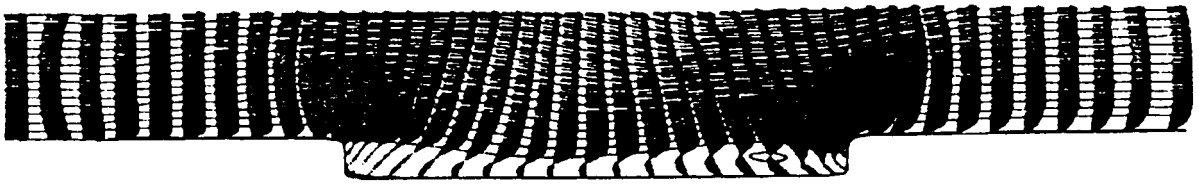

STREAMLINE CONTOURS MIN VALUE= -.1119 MAX= 1.7871
CAVITY FLOW.L/D=12.0. RE=2.0E6
90 X 70 GRID M = 1.500

(a)

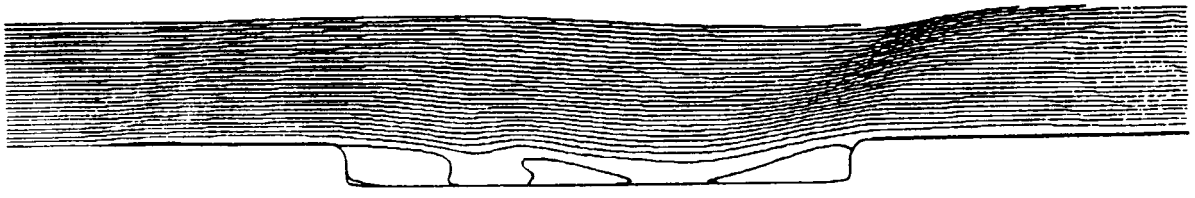

(b)

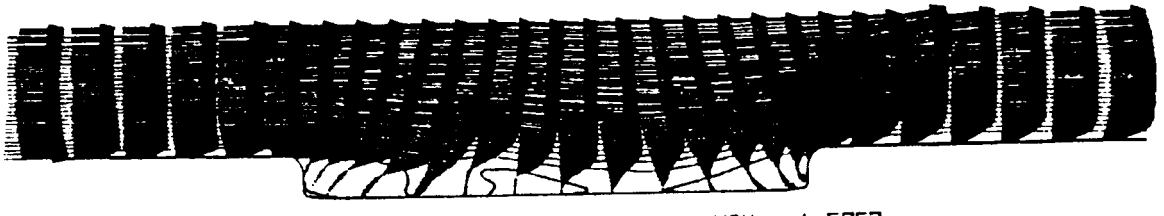

STREAMLINE CONTOURS MIN VALUE= -.0320 MAX= 1.5757
CAVITY FLOW.L/D=12.0. RE=2.0E6
90 X 70 GRID M = 1.500

(C)

Figure 18. continued

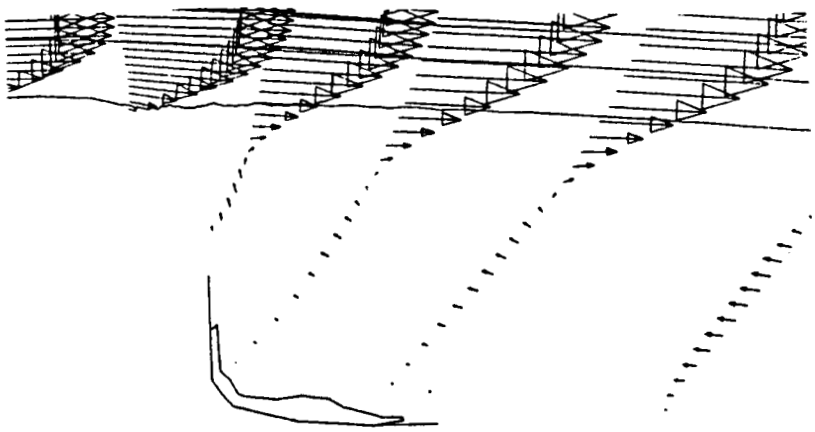

(d)

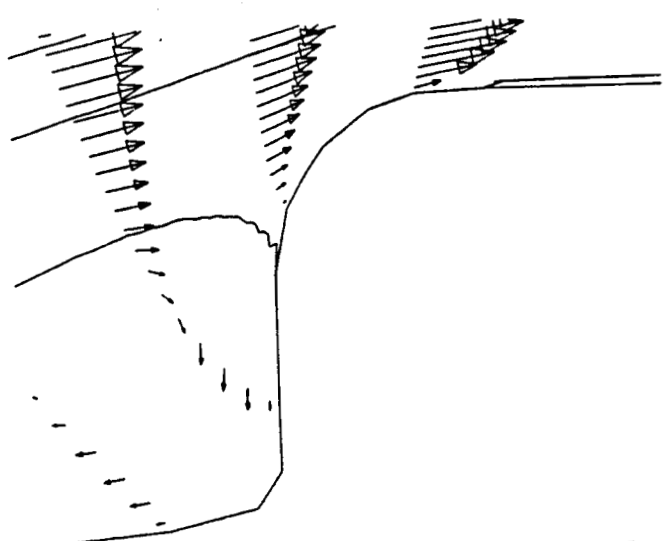

(e)

Figure 18. Supersonic flow over L/D = 12.0 cavity; (a) velocity vectors at an earlier stage of flow development, (b-c) streamlines and velocity vectors of developed flowfield, (d-e) Blow ups of corner flows.

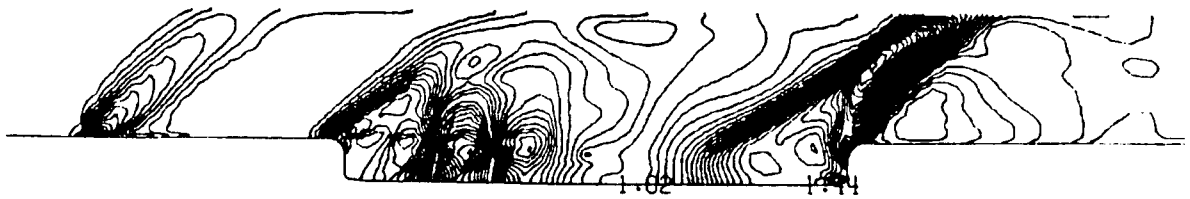

STAT PRESS CONTOURS MIN VALUE= .6483 MAX= 1.6489
CAVITY FLOW.L/D=12.0. RE=2.0E6
90 X 70 GRID M = 1.500

(a)

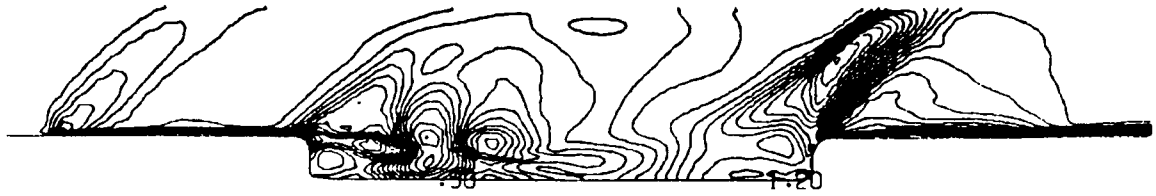

DENSITY CONTOURS MIN VALUE= .4672 MAX= 1.4166
CAVITY FLOW.L/D=12.0. RE=2.0E6
90 X 70 GRID M = 1.500

(b)

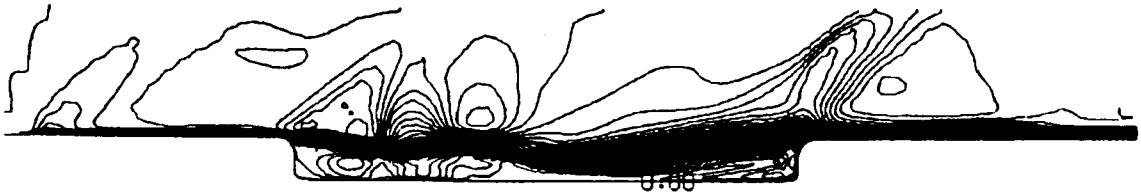

MACH CONTOURS MIN VALUE= 0.0000 MAX= 1.7358
CAVITY FLOW.L/D=12.0. RE=2.0E6
90 X 70 GRID M = 1.500

(c)

Figure 19. Supersonic flow over L/D = 12.0 cavity: (a) pressure contours, (b) density contours, (c) Mach number contours.

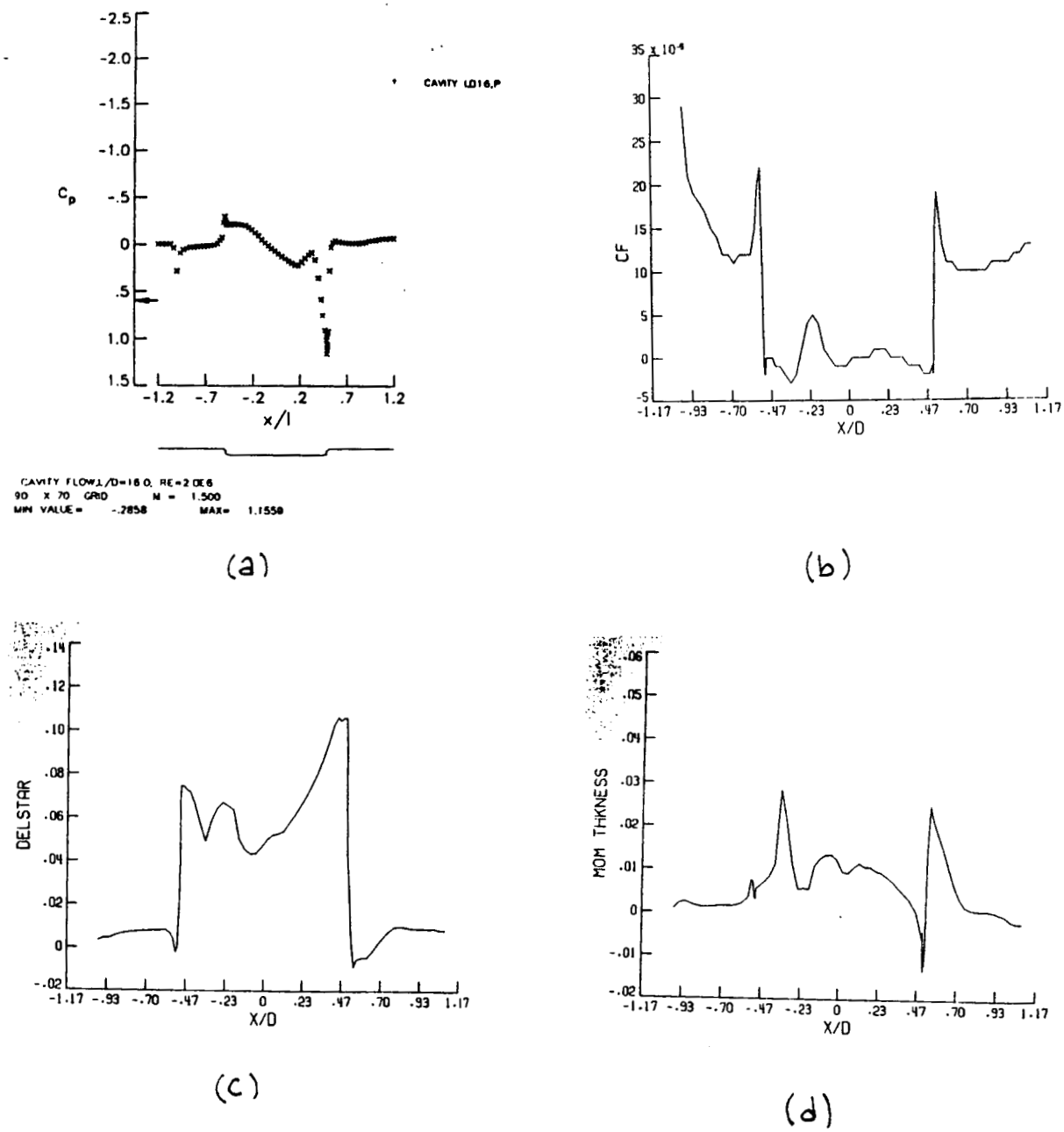

Figure 20. Supersonic flow over L/D = 16.0 cavity: (a) pressure coefficient, (b) skin friction coefficient, (c) displacement thickness, (d) momentum thickness, distributions.

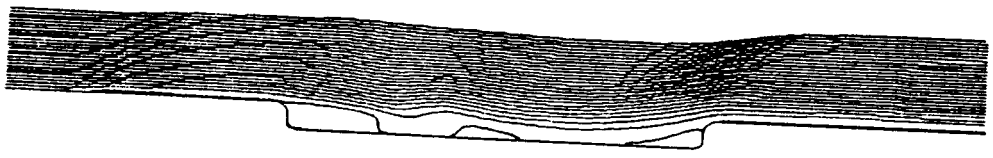

(a)

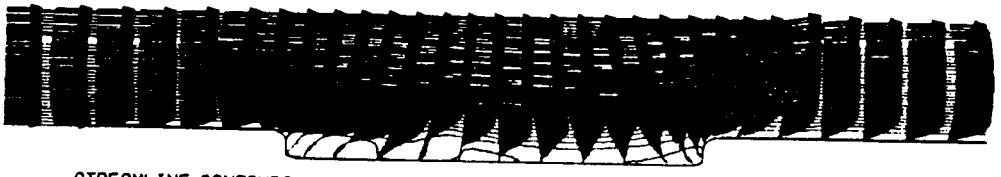

(b)

Figure 21. continued

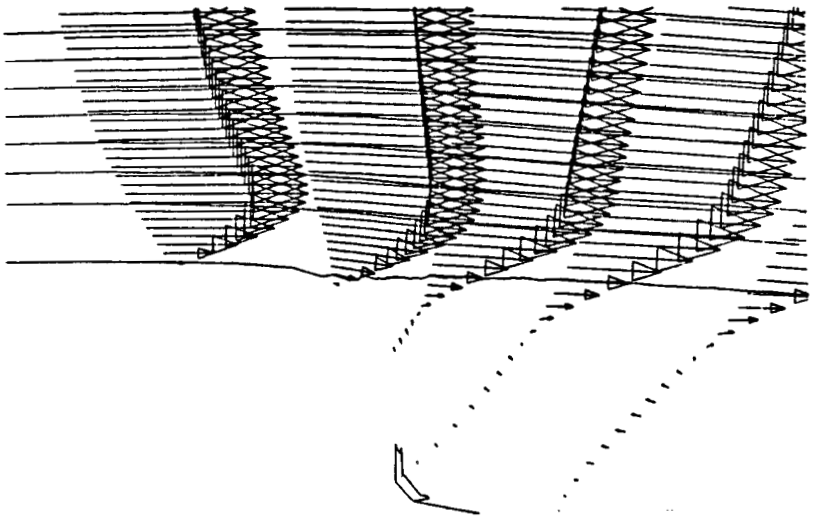

STREAMLINE CONTOURS MIN VALUE= -.1972 MAX= 18.4660
CAVITY FLOW,L/D=16.0, RE=2.0E6,
90 X 70 GRID M = 1.500

(c)

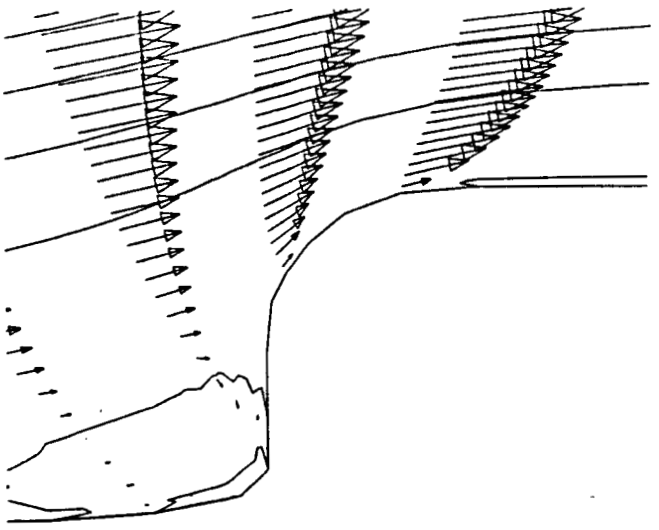

STREAMLINE CONTOURS MIN VALUE= -.2630 MAX= 24.6213
CAVITY FLOW,L/D=16.0, RE=2.0E6,
90 X 70 GRID M = 1.500

(d)

Figure 21. Supersonic flow over L/D = 16.0 cavity: (a) streamline contours, (b) velocity vectors of complete flowfield, (c-d) Blow ups of corner flows.

STAT PRESS CONTOURS MIN VALUE= .6825 MAX= 1.4927
CAVITY FLOW.L/D=16.0. RE=2.0E6.
90 X 70 GRID M = 1.500

(a)

DENSITY CONTOURS MIN VALUE= .4758 MAX= 1.2695
CAVITY FLOW.L/D=16.0. RE=2.0E6
90 X 70 GRID M = 1.500

(b)

MACH CONTOURS MIN VALUE= 0.0000 MAX= 1.7058
CAVITY FLOW.L/D=16.0. RE=2.0E6.
90 X 70 GRID M = 1.500

(c)

Figure 22. Supersonic flow over L/D = 16.0 cavity: (a) pressure contours, (b) density contours, (c) Mach number contours.

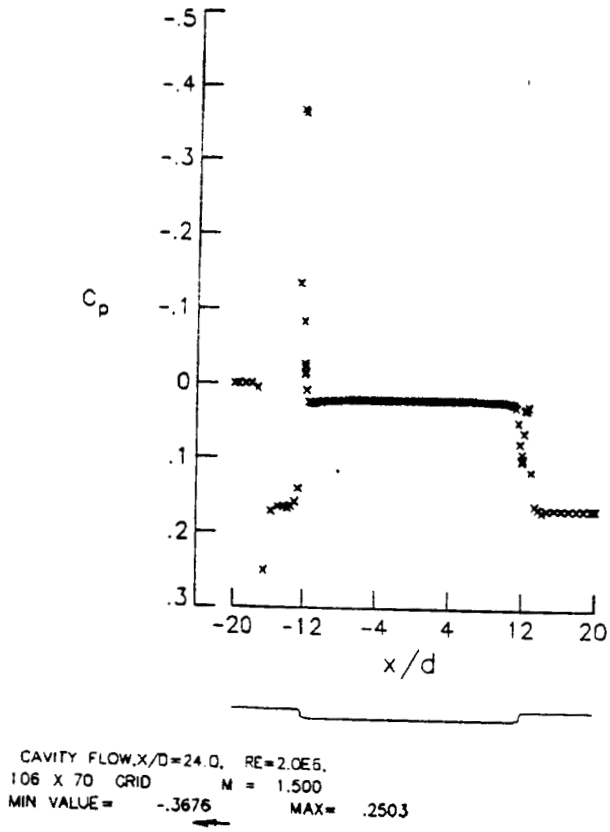

(a)

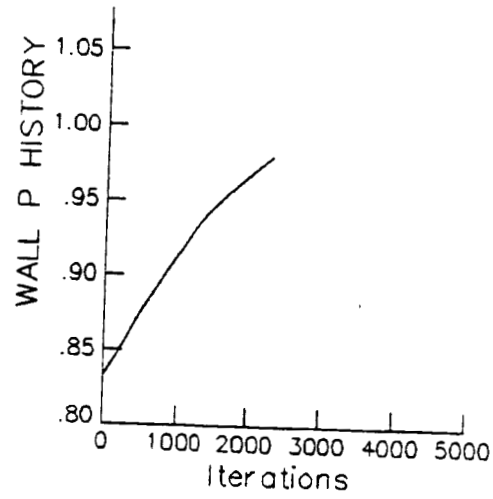

(b)

Figure 23. continued

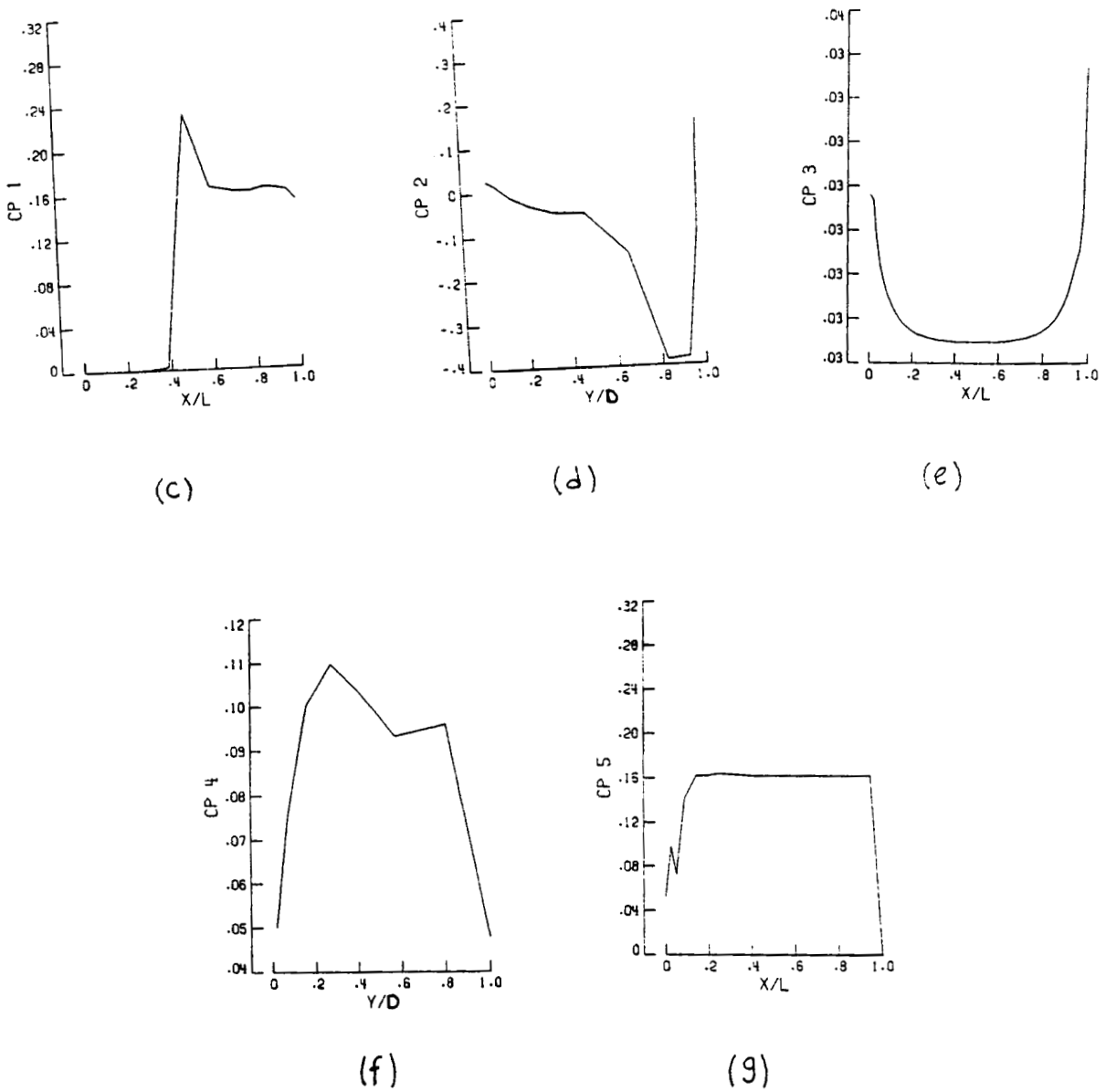

Figure 23. Supersonic flow over L/D = 24.0 cavity: (a) pressure coefficient distribution over entire wall, (b) skin friction coefficient distribution over entire wall, (c-g) pressure coefficient distribution on front flat plate (S_{FP1}), forward face (S_{FF}), ceiling (S_C), rearward face (S_{RF}), rear flat plate (S_{FP2}), respectively. (See Fig. 10 for comparison).

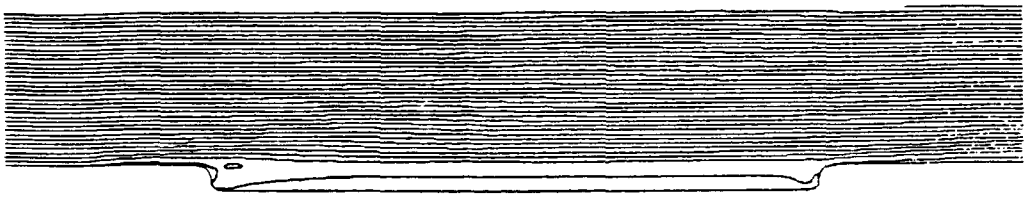

STREAMLINE CONTOURS MIN VALUE= -.0136 MAX= 2.1008
CAVITY FLOW.X/D=24.0. RE=2.0E6.
106 X 70 GRID M = 1.500

(a)

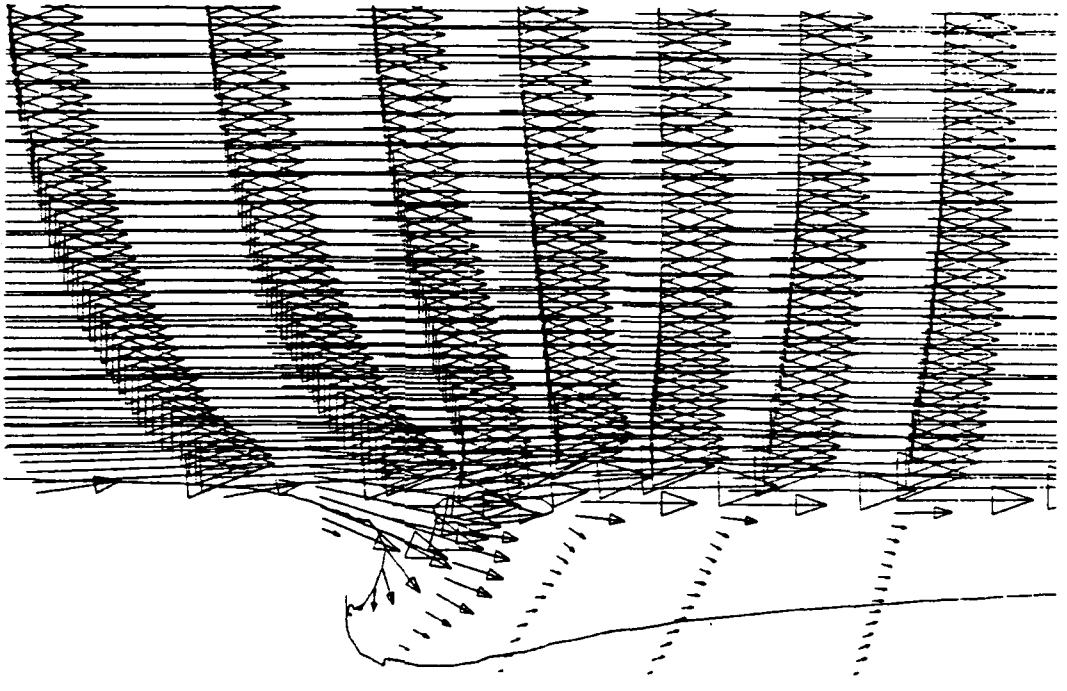

STREAMLINE CONTOURS MIN VALUE= -.0909 MAX= 14.0055
CAVITY FLOW.X/D=24.0. RE=2.0E6.
106 X 70 GRID M = 1.500

(b)

Figure 24. continued

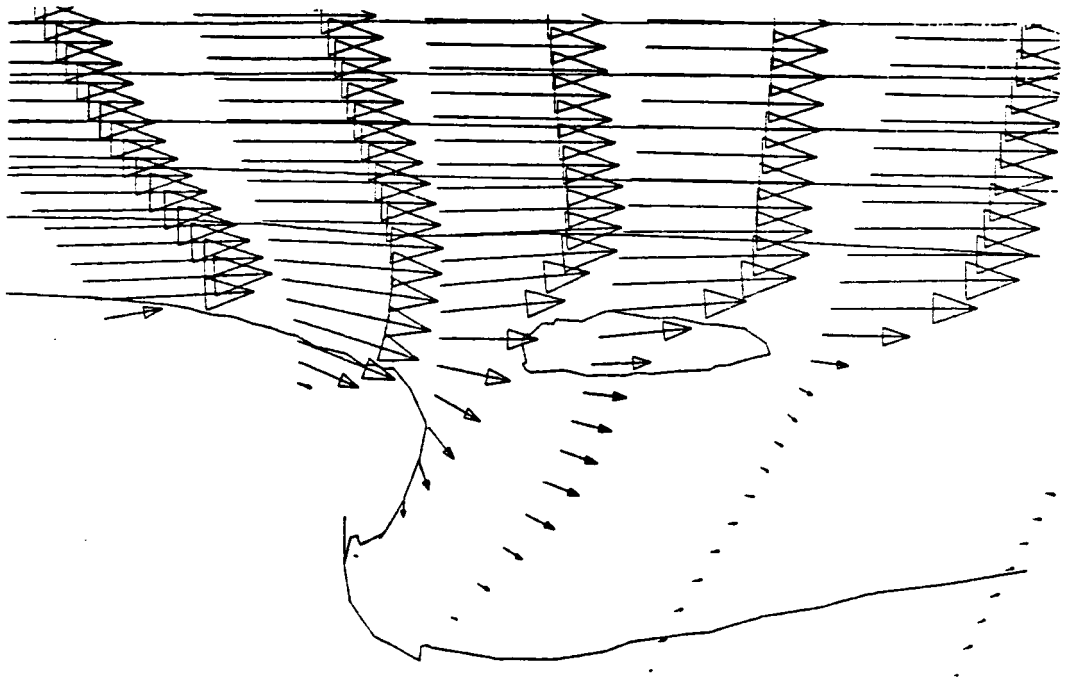

STREAMLINE CONTOURS MIN VALUE= -.1817 MAX= 28.0109
CAVITY FLOW.X/D=24.0. RE=2.0E6.
106 X 70 GRID M = 1.500

(c)

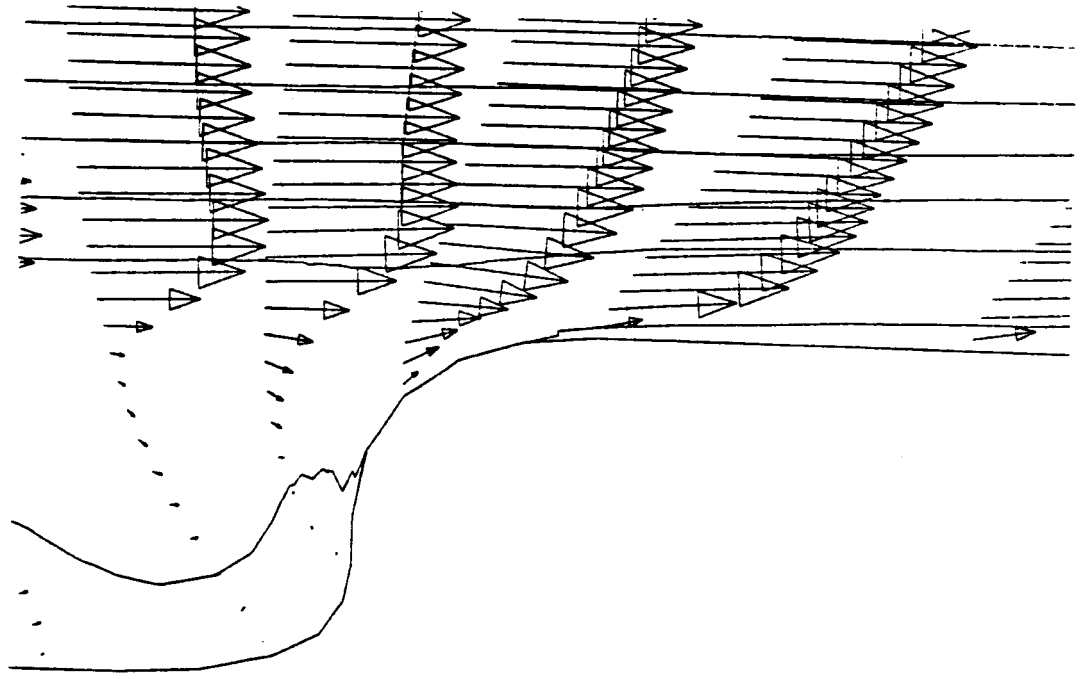

STREAMLINE CONTOURS MIN VALUE= -.1817 MAX= 28.0109
CAVITY FLOW.X/D=24.0. RE=2.0E6.
106 X 70 GRID M = 1.500

(d)

Figure 24. Supersonic flow over L/D = 24.0 cavity: (a) streamline contours, (b) velocity vectors, (c-d) blow ups of corner flows.

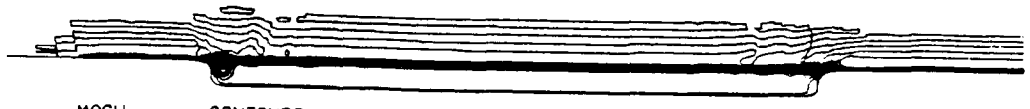

MACH CONTOURS MIN VALUE= 0.0000 MAX= 1.8436
CAVITY FLOW.X/D=24.0. RE=2.0E6.
106 X 70 GRID M = 1.500

(a)

STAT PRESS CONTOURS MIN VALUE= .4176 MAX= 1.4201
CAVITY FLOW.X/D=24.0. RE=2.0E6.
106 X 70 GRID M = 1.500

(b)

DENSITY CONTOURS MIN VALUE= .2903 MAX= 1.2402
CAVITY FLOW.X/D=24.0. RE=2.0E6.
106 X 70 GRID M = 1.500

(c)

Figure 25. Supersonic flow over L/D = 24.0 cavity: pressure contours, (b) density contours, (c) Mach number contours.

APPENDIX
DETAILS OF MACCORMACK SCHEME ADAPTATION

$$A = \begin{bmatrix} 0 & \xi_x & \xi_y & 0 \\ -u U_\xi + \xi_x \beta \alpha & U_\xi - (\beta-1)\xi_x u & \xi_y u - \beta \xi_x v & \beta \xi_x \\ v U_\xi + \xi_y \beta \alpha & -\beta \xi_y u + \xi_x v & U_\xi - (\beta-1)\xi_y v & \beta \xi_y \\ A_{41} & A_{42} & A_{43} & (\beta+1) U_\xi \end{bmatrix}$$

where

$$A_{41} = U_\xi \left[\alpha(\beta-1) - \frac{a^2}{\beta}\right]$$

$$A_{42} = -\beta U_\xi u + \left[\frac{a^2}{\beta} + \alpha\right] \xi_x$$

$$A_{43} = -\beta U_\xi v + \left[\frac{a^2}{\beta} + \alpha\right] \xi_y$$

$$\alpha = \frac{1}{2}(u^2 + v^2)$$

$$\beta = (\gamma-1)$$

$$a = \sqrt{\gamma p/\rho}$$

$$\xi_x = \partial\xi/\partial x$$

$$\xi_y = \partial\xi/\partial y$$

U_ξ and U_η are contravariant velocities

$$U_\xi = u\xi_x + v\,\xi_y$$

$$U_\eta = un_x + vn_y$$

$$n_x = \partial n/\partial_x$$

$$n_y = \partial n/\partial y$$

Jacobian matrix β is obtained similarly as follows:

$$\hat{B} = \begin{bmatrix} 0 & n_x & n_y & 0 \\ -u\,U_\eta + n_x\,\beta\,\alpha & U_\eta - (\beta-1)\,n_x u. & n_y u - \beta n_x v & \beta n_x \\ v\,U_\eta + n_y\,\beta\,\alpha. & -\beta\,n_y\,u + n_x v & U_\eta - (\beta-1)\,n_y v & \beta n_y \\ B_{41} & B_{42} & B_{43} & (B+1)\,U_\eta \end{bmatrix}$$

$$B_{41} = U_\eta\left[\alpha\,(\beta-1) - \frac{a^2}{\beta}\right]$$

$$\beta_{42} = -\beta\,U_\eta\,u + \left[\frac{a^2}{\beta} + \alpha\right] n_z$$

$$A_{43} = -\beta U_\eta\,v + \left[\frac{a^2}{\beta} + \alpha\right] n_y$$

The integration scheme can be simplified by diagonalising A and B.

Once the eigenvalues of $\hat{A}$ and $\hat{B}$ are known, it is possible to express $\hat{A}$ and $\hat{B}$ in the form

$$\hat{A} = \hat{S}_\xi \Lambda_A \hat{S}_\xi^{-1}$$
$$\hat{B} = \hat{S}_\eta \Lambda_B \hat{S}_\eta^{-1}$$

where Λ_A and Λ_B are diagonal matrices consisting of the eigenvalues of $\hat{A}$, $\Lambda_{A,1} \ldots \Lambda_{A,4}$ and $\hat{B}$, $\Lambda_{B,1}, \ldots \Lambda_{B,4}$, respectively. The vectors $\hat{S}_\xi$ and $\hat{S}_\eta$ are constructed using the eigenvalues of $\hat{A}$ and $\hat{B}$, respectively, as columns.

where

$$\hat{S}_\xi = \begin{bmatrix} 1 & 0 & \frac{\rho}{\alpha\sqrt{2}} & \frac{\rho}{\alpha\sqrt{2}} \\ u & \rho\,\xi_y/c_1 & \rho\left[\frac{u}{a} + \frac{\xi_x}{c_1}\right]/\sqrt{2} & \rho\left[\frac{u}{a} - \frac{\xi_x}{c_1}\right]/\sqrt{2} \\ v & -\rho\,\xi_x/c_1 & \rho\left[\frac{v}{a} + \frac{\xi_y}{c_1}\right]/\sqrt{2} & \rho\left[\frac{v}{a} - \frac{\xi_y}{c_1}\right]/\sqrt{2} \\ \alpha & \frac{\rho\,[u\xi_y - v\xi_x]}{c_1} & \rho\left[\frac{\alpha}{a} + \frac{U_\xi}{c_1} + \frac{a}{\beta}\right]/\sqrt{2} & \rho\left[\frac{\alpha}{a} - \frac{U_\xi}{c_1} + \frac{a}{\beta}\right]/\sqrt{2} \end{bmatrix}$$

$$c_1 = \sqrt{\xi_x^2 + \xi_y^2}$$

$$\hat{S}_\xi^{-1} = T^{-1} M_\xi^{-1}$$

where $M = \begin{bmatrix} 1 & 0 & 0 & 0 \\ u & \rho & 0 & 0 \\ v & 0 & \rho & 0 \\ \alpha & \rho u & \rho v & 1/\beta \end{bmatrix}$

$$\hat{S}_\xi^{-1} = \begin{bmatrix} \dfrac{1-\alpha\beta}{a^2} & (\beta u/a^2) & (\beta v/a^2) & -\beta/a^2 \\ \dfrac{-u\xi_y + v\xi_x}{\rho c_1} & \dfrac{\xi_y}{\rho c_1} & \dfrac{-\xi_x}{\rho c_1} & 0 \\ \dfrac{\dfrac{\alpha\beta}{a} - U_\xi/c_1}{\rho\sqrt{2}} & \dfrac{\dfrac{\xi_x}{c_1} - \dfrac{\beta u}{a}}{\rho\sqrt{2}} & \dfrac{\dfrac{\zeta y}{c_1} - \dfrac{\beta v}{\alpha}}{\rho\sqrt{2}} & \dfrac{\beta}{\rho a\sqrt{2}} \\ \dfrac{\dfrac{\alpha\beta}{a} \quad \dfrac{U_\xi}{c_1}}{\rho\sqrt{2}} & - \dfrac{\dfrac{\xi_x}{c_1} + \dfrac{\beta u}{a}}{\sqrt{\rho \quad 2}} & - \dfrac{\dfrac{\xi_y}{c_1} + \dfrac{\beta v}{a}}{\sqrt{\rho \quad 2}} & \dfrac{\beta}{\rho a\sqrt{2}} \end{bmatrix}$$

$$\Lambda_A = \begin{bmatrix} U_\xi & 0 & 0 & 0 \\ 0 & U_\xi & 0 & 0 \\ 0 & 0 & U\xi + ac_1 & 0 \\ 0 & 0 & 0 & U\xi - ac_1 \end{bmatrix}$$

$$\hat{S}_\eta^{-1} = \begin{bmatrix} \dfrac{1-\alpha\beta}{a^2} & \beta u/a^2 & \beta v/a^2 & -\beta/a^2 \\ -un_y + vn_x & \eta y/\rho c_1 & -\eta_x/\rho c_1 & 0 \\ \dfrac{\dfrac{\alpha\beta}{a} - \dfrac{U_\eta}{c_1}}{\rho\sqrt{2}} & -\left[\dfrac{\dfrac{n_x}{c_1} - \dfrac{\beta u}{a}}{\rho\sqrt{2}}\right] & -\left[\dfrac{\dfrac{\eta_y}{c_1} - \dfrac{\beta_v}{a}}{\rho\sqrt{2}}\right] & \dfrac{\beta}{\rho a\sqrt{2}} \end{bmatrix}$$

$$\hat{S}_\eta = \begin{bmatrix} 1 & 0 & \rho/a\sqrt{2} & \rho/a\sqrt{2} \\ u & \rho\, n_y/c_1 & \rho\left[\frac{u}{a} + \frac{n_x}{c_1}\right]/\sqrt{2} & \rho\left[\frac{u}{a} - \frac{n_x}{c_1}\right]/\sqrt{2} \\ v & -\rho\, n_x/c_1 & \rho\left[\frac{v}{a} + \frac{n_y}{c_1}\right]/\sqrt{2} & \rho\left[v/a - \frac{n_y}{c_1}\right]/\sqrt{2} \\ \alpha & \rho\left[\frac{um_y - v\, n_x}{c_1}\right] & \rho\left[\frac{\alpha}{a} + \frac{U_\eta}{c_1} + \frac{a}{\beta}\right]\sqrt{2} & \rho\left[\frac{\alpha}{a} - \frac{U_\eta}{c_1} + \frac{a}{\rho}\right]/\sqrt{2} \end{bmatrix}$$

$$\Lambda_\beta = \begin{bmatrix} U_\eta & 0 & 0 & 0 \\ 0 & U\eta & 0 & 0 \\ 0 & 0 & U_\eta + ac_1 & 0 \\ 0 & 0 & 0 & U_\eta - ac_1 \end{bmatrix}$$

The matrices $|\hat{A}|$ and $|\hat{B}|$ are formed by replacing the matrices Λ_A and Λ_B by positively valued diagonal matrices D_A and D_B such that

$$D_A = |\Lambda_A| + \lambda_A I.$$

$$D_B = |\Lambda_B| + \lambda_B I.$$

where $$\lambda_A = \frac{2\nu}{\rho\Delta\xi}\left[\xi_x{}^2 + \xi_y{}^2\right] - \frac{1}{2}\frac{\Delta\xi}{\Delta t}.$$

$$\lambda_B = \frac{2\nu}{\rho\Delta\eta} \left(\eta_x^2 + \eta_y^2 \right) - \frac{1}{2} \frac{\Delta\eta}{\Delta t}$$

$$\nu = \max \left[\mu, (\lambda+2\mu), k \right]$$

The expressions for D_A and D_B assume that viscous effects are modeled in the implicit part of the scheme by the addition of the terms λ_A, λ_B which include viscosity through the coefficient. ν.